

Using astrochemical models to simulate reactivity experiments on cold surfaces

Valeriia Sokolova,^{*,†} Basile Husquinet,^{‡,†} Stephan Diana,[†] Paola Caselli,[‡]
Emanuele Congiu,[†] Wiebke Riedel,[‡] Olli Sipilä,[‡] Anton Vasyunin,[¶] Valentine
Wakelam,[§] and Francois Dulieu^{*,†}

[†]*CY Cergy Paris Université, Observatoire de Paris, Université PSL, Sorbonne Université,
Université Paris Cité, CNRS, LIRA, F-95000, Cergy, France*

[‡]*Center for Astrochemical Studies, Max-Planck-Institute for Extraterrestrial Physics (MPE),
Gießenbachstr. 1, D-85748 Garching, Germany*

[¶]*Research Laboratory for Astrochemistry, Ural Federal University, Kuibysheva St. 48
Yekaterinburg 620026, Russia*

[§]*Laboratoire d'astrophysique de Bordeaux, Univ. Bordeaux, CNRS, B18N, allée Geoffroy
Saint-Hilaire, 33615 Pessac, France*

E-mail: valeriia.sokolova@cyu.fr; francois.dulieu@cyu.fr

Abstract

The development of molecular complexity during stellar and planetary formation owes much to the interaction of gas and dust. When the first astrochemical models including solid-state chemistry were developed more than forty years ago, data from dedicated laboratory experiments were limited. Since then, many groups have developed specific experimental set-ups to address this issue, but astrochemical models have rarely been directly confronted with these new results. We want to demonstrate whether it is possible to use rate-equation-type

astrochemical models developed in the context of the Interstellar Medium to compare them with laboratory astrophysics experiments.

In this work, we use the case of low-temperature hydrogenation of CO, which is known to lead to methanol, among other molecules. We carried out 9 experiments, varying the experimental parameters such as temperature and dose. We give quantitative results and take care of detailing the vocabulary used in the experiments. We use astrochemical codes, NAUTILUS, pyRate and MONACO, to reproduce our experimental conditions, which requires good control of the change of vocabulary and scales, especially for fluxes and time scales.

This work demonstrates that it is possible to use different astrochemical codes to compare modelling results directly with the output of experiments. There are discrepancies between models and experiments, as well as between models, but a fair agreement is achieved. We discuss the possible origin of the differences, which could originate from the chemical network or the difference in the description of physical processes.

Keywords

Astrochemistry, Molecular processes, Laboratory astrophysics, Numerical modelling, ISM: molecules

Introduction

Dust particles play an important role in the astrophysics of the interstellar medium, from thermodynamics and chemical processes to the dynamics of star formation. The chemical composition of dust particles depends on the initial chemical composition of the environment where dust particles were formed: there are silicate and graphite particles, particles consisting of silicon carbide, etc.¹

Within the dense regions of the interstellar medium (ISM), such as molecular clouds, cores, and denser objects, where the temperatures are low and the number densities of particles in gas are high, species adsorb to the surface of dust grains and can easily form molecular ices. The composition of ice mantles is complex and includes significant amounts of carbon monoxide (CO),

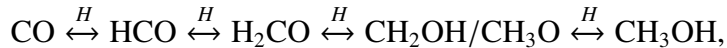
carbon dioxide (CO_2), water (H_2O), methanol (CH_3OH), ammonia (NH_3) and possibly complex molecules.^{2–4} These ices are formed under very cold conditions, typically below 100 K and even below 10 K, and are influenced by cosmic rays, UV radiation, and the processes of accretion and desorption. Studying the dust ice mantles is one of the important questions in modern laboratory astrochemistry: understanding the composition and behaviour of ice is pivotal for further exploration of processes that govern the chemical and physical evolution of the ISM.

In recent years, many attempts have been made to understand how complex organic molecules and astrochemical ices can be formed on the surfaces of ice and dust by combining observations,^{5–8} chemical modeling,^{9–14} and laboratory experiments.^{15–20} Laboratory experiments include the experimental studies as well as the quantum-chemical and molecular dynamics calculations.²¹ This approach can be considered as a bridge between observations and the theoretical part of studies, providing data derived from controlled experiments on special setups for both fields. Such setups are capable of recreating conditions of the ISM and allow scientists to simulate and study complex chemical processes that can happen in space. One of the main questions that laboratory astrochemistry can answer is what type of molecules we expect to see and actually detect in space.²² From experimental studies, we can obtain data about compounds that can be found in spectroscopy in the range from UV to mm wavelengths and compare it with data that is provided from observations. In addition to that, a lot of information about chemical reactions can be derived: for example, binding energies of compounds (e.g. Perrero et al.²³) and activation energies of reactions, reaction rates etc.

Theoretical studies of the chemical evolution of the ISM include computational codes that implement various mathematical methods for calculating reaction rates, atomic and molecular abundances, etc. All astrochemical codes use chemical reaction databases that are based on the results of laboratory studies. Currently, the most common databases are UMIST 2013 (for gas-phase reactions)^{24,25} and KIDA (which takes into account not only gas-phase reactions but also reactions on the surface of dust particles and their ice mantles).^{26–28}

In this work, we focus on the study of the solid-state chemical evolution of atoms and molecules

in the {CO+H} chemical system by a combination of laboratory experiments and astrochemical modeling. The hydrogenation of CO on the surface of dust particles is one of the most well-studied processes in astrochemistry and can be considered as a benchmark for chemistry on grain surfaces, thanks to its simplicity.²⁹ The hydrogenation of CO can eventually lead to the formation of formaldehyde and methanol through the sequence of reactions:³⁰⁻³⁵



where forwards and backwards arrows indicate the H-addition and H-abstraction reaction, respectively. These reactions were carefully studied using a combination of laboratory experiments and theoretical approaches such as quantum chemical calculations and simple chemical modeling. However, despite all efforts, our understanding of this process is still not complete. In the past years it was discovered that the standard scenario of CH₃OH formation is missing some of the "reverse" reactions for HCO and H₂CO,³⁴ leading not only to the new destruction paths, but also to the unexpected effect of non-thermal desorption of compounds,³⁶ except for HCO,³⁷ which adds some constraints to the hydrogenation path. In following years, each step of the chain was revised, adding more and more information about activation energies, branching ratios and other important parameters for the reaction rate calculations.³⁸ From the theoretical point of view, the research was focused both on quantum calculations and classical modelling of CO chemical evolution. Rimola et al.²⁹ were the first to combine a quantum approach (based on the density functional theory (DFT) approach), deriving energy barriers and transition frequencies, with macroscopic astrochemical modelling (based on the rate equations approach), where they implemented this data. Later on Enrique-Romero et al.^{39,40} studied the activation energy barriers of radical-radical interactions including the {CO+H} system. In following studies, the research was focused on using the rate equations approach, studying new mechanisms involved in the chain (e.g., non-diffusive mechanisms⁴¹), applying all theoretical data to the modelling of the ISM objects of interest.⁴²⁻⁴⁴

This paper is organized as follows: Section Experimental methods, vocabulary and results

is dedicated to laboratory measurements and description of experiments, Section Rate-equations approach describes the theoretical approach that we used, in Sections MONACO code and results, NAUTILUS code and results and pyRate code and results we present the results of astrochemical modelling using different popular codes, and in the Section Conclusion we summarize all the results.

Experimental methods, vocabulary and results

For this project, we use the special laboratory setup that provides controlled conditions that mimic those in space — VENUS, from the acronym VErs des NoUvelles Synthèses ("Towards new syntheses" in French). The full description of the setup with all details can be found in Congiu et al.⁴⁵.

The VENUS setup can provide very low temperatures for the experiments (5 - 8 K with the proper shielding) and ultra-high vacuum. The lowest pressure that can be obtained is 2×10^{-11} mbar, but the usual one that is used for the experiments is 10^{-10} mbar, which corresponds to a gas density of $\simeq 3 \times 10^6$ particles per cm^3 , mostly composed of H_2 , with traces of others UHV pollutants such as, by decreasing partial pressure CO , CO_2 , H_2O , Ar , CH_4 , and other hydrocarbons.⁴⁵ These values are good enough to mimic conditions for the solid-state synthesis of molecules in the interstellar medium and allow surface-surface and gas-surface reactions to dominate over gas-gas collisions. For studying the formation and destruction of molecules a quadrupole mass-spectrometer (QMS) and an infrared spectrometer (that implements vibrational fingerprint spectra in the mid-infrared domain 2.5 - 15 μm) were placed in the Main Chamber. The full scheme of the setup is presented in the Fig. 1.

The setup was designed to study very thin systems (from sub-monolayers to several monolayers) where molecules can react on the cold gold-coated surface with a typical collision rate of 10^{12} particles $\text{cm}^{-2}\text{s}^{-1}$. All molecules are injected in the chamber in gaseous form, originally coming from liquids, gases or solids.

Up to 4 species can be put in the system with the multi-beam stage, containing the right beam

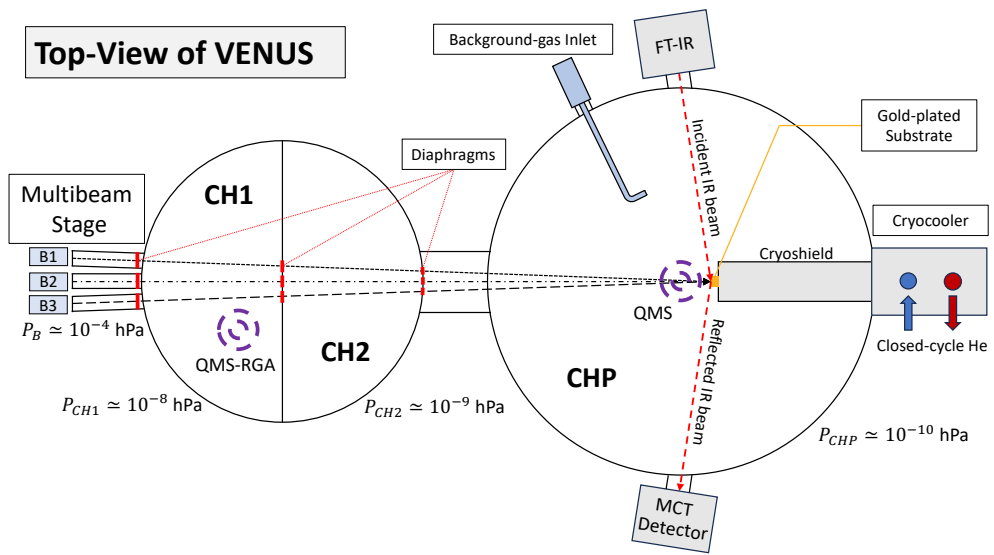


Figure 1: Simplified schematic top view of the VENUS Setup. From left to right: multibeam stage for species injection in the system, intermediate chamber (CH1 and CH2) for preparation of the beams, main chamber with gold-coated sample inside of it, QMS for detection of gas-phase species (place in front of the sample during the TDP), FT-IR detector for controlling the growth of the ices, and cryostat that regulates the temperature in the system. Source: Husquinet et al.⁴⁶. Reprinted with permission from [Husquinet et al., A&A, 703, A16 (2025) <https://doi.org/10.1051/0004-6361/202554408>] published under the terms of the Creative Commons Attribution License (<https://creativecommons.org/licenses/by/4.0>). Copyright 2025, Astronomy and Astrophysics.

(B3), the top beam (B1), the central beam (B2) and the left beam (not in use at this moment), which is shown in the Fig. 1. These beam lines have typical accretion flux at the surface of 1.67×10^{12} molecules $\text{cm}^{-2}\text{s}^{-1}$ that gives for example 1 ML of CO ice growing on the gold plate surface in approx. 10 minutes.⁴⁵ Here and later all deposition doses will be quantified in monolayers (ML), and 1 ML is 1×10^{15} molecules cm^{-2} that corresponds to the number of adsorption sites per cm^{-2} on the surface and has a physical meaning of one layer of product that covers the surface without desorbing (for example, CO at surface temperatures below 23 K). H atoms have low binding energy and high reactivity, so in that case an accretion of 1 ML of H does not mean that one layer of H atoms is present on the surface. Instead, we accept that statistically each adsorption site has been exposed to one H atom coming from the gas phase.

The general experiment consists of two steps: deposition of species on the surface (step 1) and sublimation of the evolved species in the gas during the linear increase of the surface temperature (step 2), usually Temperature Programmed Desorption (TPD).

The gold-coated copper sample in the main chamber is attached to the Helium cryostat's cold finger, which allows to keep a constant temperature during the whole time of the deposition. Deposited molecules come to the surface, and form the ice film, and during this step, they can be constantly monitored with Fourier transform reflection-absorption infrared spectroscopy (FT-RAIRS). This technique is used for analysing the chemical evolution from the moment of molecule deposition on the sample surface until the formation of new products and ices. Hence composition, thickness and morphology of ices can be studied "on the go". One saved infrared spectrum contains 256 averaged scans, corresponding to an acquisition time of approx. 2 min.⁴⁵ Figure 2 presents the first spectra obtained during CO deposition on a surface held at 10 K for 10 min deposition on a bare gold surface (corresponding to experiment # 1 of Table 1 and to sketch A of Figure 4). The column density of the adsorbate can be deduced from the area of the IR absorption peaks. In this case it corresponds to a linear quantity increase of CO on the surface.

The FT-RAIRS technique is combined with the TPD for better control of the evolution of chemical compounds on the sample surface. The TPD is a powerful tool for monitoring interactions

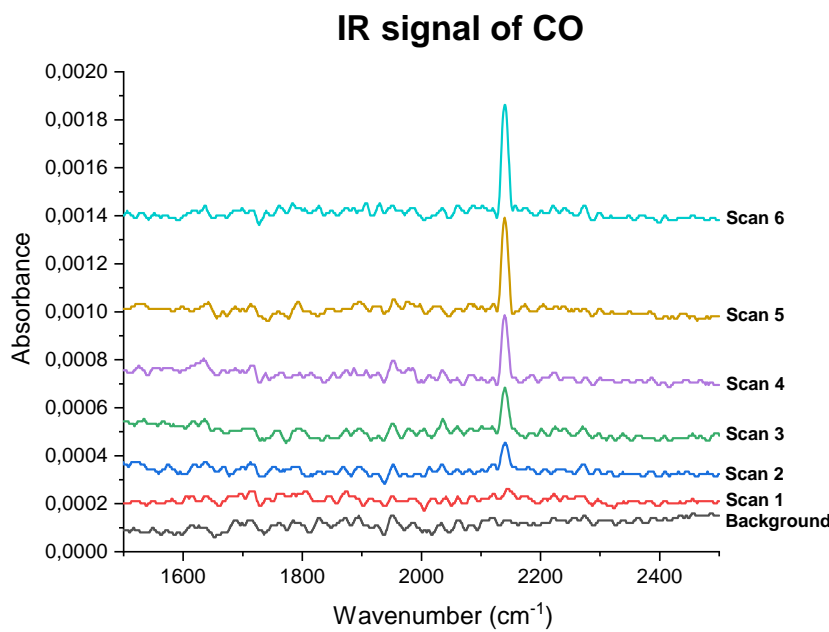


Figure 2: Family of infrared spectra for a CO deposition of 10 minutes on the gold surface held at 10 K (corresponding to experiment # 1 of Table 1 and A) on Fig. 4). Scanning starts with the background spectrum and continues for the whole time of the deposition. Spectrum 6 refers to the additional scan made after the deposition was stopped, corresponding to 1.0 ML. A strong peak is visible at around 2140 cm^{-1} . Signals have been vertically offset for better visibility.

of molecules on the surface during the controlled changing of the sample temperature. During the TPD, temperature is linearly increasing with a rate of 0.2 K s^{-1} and can be varied from 8 to 400 K.⁴⁵ All desorbing species are measured with the Hiden 51/3F vertically translatable quadrupole mass spectrometer which can monitor several masses at the same time and give the intensity of each chosen mass as a function of temperature. During this stage, QMS is placed at 5 mm in front of the surface. This method provides information about the desorption temperatures (hence, indirect access to binding energies) of molecules and the quantity of these adsorbed molecules (from the intensity of the TPD spectrum peaks).

In our experiments, we varied the TPD from surface temperature (9—15 K) to 200 K with a ramp of 0.2 K/s. Figure 3 shows the TPD spectrum of experiment #4, displaying the main masses of CO ($m/z=28$), H₂CO ($m/z=30$), and CH₃OH ($m/z=31$). The abundances of each molecule (N_x) in Table 1 are calculated using the following equation:

$$N_x = \frac{A_x}{A_{CO}^{ML}} \frac{\sigma_{CO}^{Tot}}{\sigma_x^{Tot}}, \quad (1)$$

where A_x represents the area of the TPD spectrum of molecule X , taking into account the cracking pattern (see Vitorino et al.⁴⁷). A_{CO}^{ML} denotes the area of a CO monolayer, while σ_x^{Tot} signifies the total cross section for electron impact ionization (at 30 eV, the value we use) for molecule X and σ_{CO}^{Tot} for CO. The total cross-section for CO is $\sigma_{CO}^{Tot} = 1.296 \text{ \AA}^2$,⁴⁸ for H₂CO $\sigma_{H_2CO}^{Tot} = 2.74 \text{ \AA}^2$,⁴⁹ and for CH₃OH $\sigma_{CH_3OH}^{Tot} = 3.263 \text{ \AA}^2$.⁵⁰ The sensitivity of the QMS by mass is not considered here, as the masses of the studied molecules are very similar (28 m/z to 32 m/z), which has a negligible impact on the final result. As H₂CO and CH₃OH are the products of CO, the estimated monolayer (ML) abundance of the products is calculated as a function of CO.

In addition, the TPD technique allows to calibrate the flux of the molecules. In the case of CO, the molecular beam calibration was performed as described in Congiu et al.⁴⁵ and Kruczkiewicz et al.⁵¹. To calibrate the CO flux on our setup, we deposit CO on the surface for different time periods, corresponding to different doses, and then perform the TPD. From the TPD shapes the

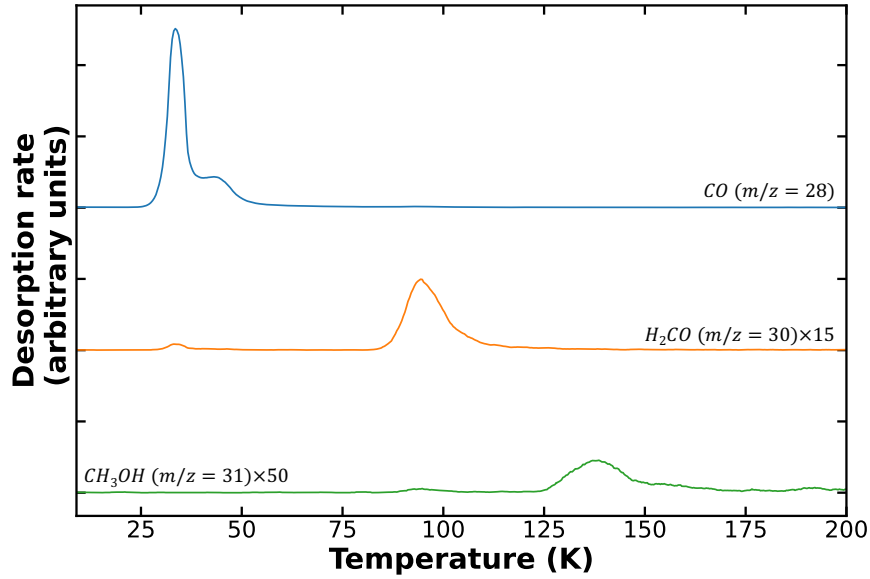


Figure 3: TPD spectra of the experiment #4, a co-deposition of CO+H on a surface held at 9 K, where the top spectra in blue represent CO ($m/z=28$), H₂CO is represented in the orange spectra in the middle and the CH₃OH ($m/z=31$) in the bottom with the green spectra. Given the low levels of H₂CO and CH₃OH production, the spectra were multiplied by factors of $\times 15$ and $\times 50$, respectively.

transition from the first to the second layer can be determined. For this calibration the surface temperature is fixed during depositions to guarantee the homogeneous distribution of molecules on the surface. For our experiments, we estimate that 1 ML of CO ice is formed in 10 minutes using a flow rate of 0.03 sccm (standard cubic centimetres per minute, quantifies the flow rate) in the source, and $T_{surf} = 10$ K, which gives us a flux equal to :

$$\phi_{CO} = \frac{10^{15} \text{molecules cm}^{-2}}{600 \text{s}} \simeq 1.67 \times 10^{12} \text{molecules cm}^{-2} \text{s}^{-1} \quad (2)$$

For the flux of H atoms, we dissociate H₂ by creating a plasma in the quartz tube, surrounded by the microwave cavity (see details in Vitorino et al.⁴⁷). In that case, the absolute calibration uncertainty of flux is larger because it is based on H reactivity in multi-reaction systems that are supposed to be barrierless: for example, {O₂+H} or {NO+H}.⁵² In our settings, one ML of H atoms can be achieved in about 2.5 minutes (time to consume O₂ molecules), with flux $\phi_H = 6.67 \times 10^{12} \text{atoms cm}^{-2} \text{s}^{-1}$ as can be seen in Table 1.

The absolute calibration of molecular fluxes (such as CO) has uncertainties, usually estimated

to be around 15%. For atoms, there are underlying assumptions that enlarge the absolute calibration error. However, the reproducibility of the fluxes have an accuracy of less than 5%. From one product to another, the main source of uncertainty is the knowledge of ionisation cross-section. Thus, if the relative calibration between compounds may vary approximately by 15%, the quantity of the same species is accurately known and can be compared from one experiment to another.

For this project, we performed the CO hydrogenation experiments shown in Table 1. Figure 4 represents the visual form of these experiments. The notation is as follows: if two species are deposited together at the same time (co-deposition), we put both species in curly brackets $\{\text{CO} + \text{H}\}$, and if there was a sequential deposition (one after another), it is noted as $\{\text{CO}\} + \{\text{H}\}$.

Table 1: List of experimental results from TPD at the end of the deposition.

| # | Experiments | Deposit Time (minutes) | Ts (K) | ϕ_{CO} (ML/s) | ϕ_H (ML/s) | N_{CO} (ML) | N_{H_2CO} (ML) | N_{CH_3OH} (ML) | Radical (ML) | COMs | Missing (ML) |
|-----------------|----------------------------------|---------------------------|-----------|-----------------------|--------------------|------------------|---------------------|----------------------|-----------------|------|-----------------|
| 1 | $\{\text{CO}\}$ | 10 | 10 | 1.67(-3) | 0 | 1.0 | 0 | 0 | 0 | No | 0 |
| 2 | $\{\text{CO}+\text{H}\}^a$ | 15 | 10 | 1.67(-3) | 6.67(-3) | 0.73 | 0.11 | 0.097 | <0.1 | No | 0.56 |
| 3 | $\{\text{CO}\}$ | 60 | 15 | 1.85(-3) | 0 | 6.667 | 0 | 0 | 0 | No | 0 |
| 4 ^d | $\{\text{CO}+\text{H}\}^a$ | 60 | 9 | 1.85(-3) | 3.34(-3) | 4.063 | 0.169 | 0.039 | <0.1 | No | 2.396 |
| 5 ^d | $\{\text{CO}+\text{H}\}^a$ | 60 | 10 | 1.85(-3) | 3.34(-3) | 4.478 | 0.105 | 0.031 | <0.1 | No | 2.053 |
| 6 ^d | $\{\text{CO}+\text{H}\}^a$ | 60 | 11 | 1.85(-3) | 3.34(-3) | 5.948 | 0.053 | 0.021 | <0.1 | No | 0.645 |
| 7 ^d | $\{\text{CO}+\text{H}\}^a$ | 60 | 12 | 1.85(-3) | 3.34(-3) | 6.448 | 0.036 | 0.015 | <0.1 | No | 0.167 |
| 8 | $\{\text{CO}+\text{H}\}^a$ | 60 | 15 | 1.85(-3) | 3.34(-3) | 6.593 | 0.018 | 0.010 | <0.1 | No | 0.047 |
| 9 | $\{\text{CO}\} + \{\text{H}\}^b$ | 9+120 ^c | 9 | 1.85(-3) | 3.34(-3) | 0.225 | 0.030 | 0.120 | <0.1 | Yes | 0.625 |
| 10 ^d | $\{\text{CO}\} + \{\text{H}\}^b$ | 9+75 ^c | 9 | 1.85(-3) | 3.34(-3) | 0.321 | 0.0455 | 0.095 | <0.1 | No? | 0.539 |

and Experiments columns are the index number and the type of the experiment that was done (respectively), "Deposit time" - the time frame of the experiment (the time of the deposition of reactants) and Ts is the deposition temperature of reactants. ϕ_{CO} and ϕ_H - the fluxes of CO and H respectively. N_{CO} , N_{H_2CO} , N_{CH_3OH} - quantities of CO, H₂CO and CH₃OH (respectively) on the surface in monolayers (ML).

"Radical" indicates the upper limit of both HCO and CH₂OH constrained with RAIRS. "COMs" - the presence of complex organic molecules in the TPD traces. "Missing" - the quantities of molecules that are desorbing by chemical desorption or the formation of unknown molecules. ^a Codeposition of CO and H; ^b Deposition of CO followed by deposition of H; ^c deposition time of CO + deposition time of H; ^d Experiments used for comparison in Husquinet et al.⁴⁶.

Here, CO deposition (Experiment #1) was made for calibration purposes and was taken as a starting point for all experiments below. Experiment #2 - CO hydrogenation in sub-monolayer coverage regime that leads to an enhanced chemical desorption. Experiments #4-8 show intermediate thicknesses of ice on the surface, and the surface temperature in these experiments varied between 9 and 15 K. Experiments #9 and #10 are long hydrogenation of pre-deposited CO ice. This set of

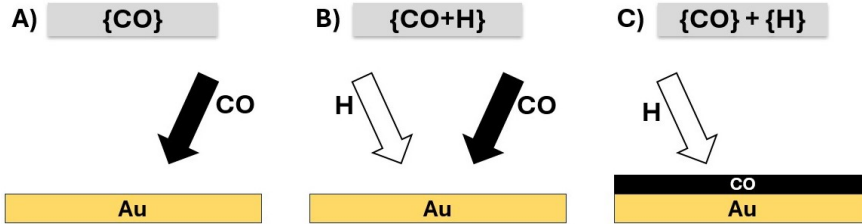


Figure 4: Schematic description of experiments shown in Table 1. CO and H are deposited on the gold-coated surface with a temperature of 10 K. From left to right: CO deposition (pic. A), co-deposition of H and CO (pic. B), sequential deposition CO and H (or hydrogenation of CO ice layer, pic. C).

experiments has been built to increase the number of experimental constraints (surface densities and temperatures) while keeping the experimental conditions coherent.

The "Missing" column in Table 1 indicates the amount of CO that is not present compared to a reference experiment. This is based on the assumption that one molecule of CO is required to produce one molecule of H_2CO and one molecule of CO for one molecule of CH_3OH . As a result, the missing column reflects chemical desorption,⁵³ or potential forms of complex organic molecules (COMs), such as methoxymethanol or glycolaldehyde. They are easily identified by their fragments HCO^+ ($m/z=29$) or CH_2OH^+ ($m/z=31$) desorbing at temperatures higher than 150 K, in addition to higher masses fragmentation patterns (such as $m/z = 61$ or 62). The determination of the chemical network of such secondary products that are only detectable in very specific conditions (long hydrogenation) is not in the scope of the current study.

The "Radical" column refers to the presence of HCO and CH_2OH in our experiments. A conservative value of 0.1 ML was adopted as the upper limit, based on the detection limit for the CO $\nu_1 = 2139 \text{ cm}^{-1}$ band. As illustrated in Figure 2, the IR spectra obtained during the CO deposition experiment reveal the emergence of the CO band starting at scan 2, which corresponds to approximately 0.2 ML of CO. Given the CO band strength $A_{\nu_1}^{\text{CO}} = 8.8 \times 10^{-18} \text{ cm/molec}$ for an IR resolution of 2 cm^{-1} and a surface temperature of 10 K,⁵⁴ the upper limit for HCO detection is estimated to be $\sim 0.1 \text{ ML}$, assuming a band strength of $A_{\nu_3}^{\text{HCO}} = 1.8 \times 10^{-17} \text{ cm/molec}$.⁵⁵ For the case of CH_2OH , since no band strength was available in the literature, the upper limit value as HCO was adopted. Figure 5 shows, as an example, the regions of the IR spectrum where these

radicals should be detected. As observed in the lower panel of Figure 5, neither the HCO nor the CH_2OH bands are visible. This observation is consistent across other spectra and experiments. These radicals are not part of the "missing" molecules because we assumed their reactions with H atoms (or other radicals) occurs too rapidly to be detected by our experimental setup. A few experimental studies have detected HCO or CH_2OH in thick ice (> 100 ML) by isolating them in chemically inert molecular matrices.^{56,57} Under our experimental conditions, we over-hydrogenate CO with a flux ratio of $\phi_{\text{CO}}/\phi_{\text{H}} = 0.25 - 0.55$, which gives the H atoms time to scan and react with all radicals present on the surface. Finally, using the combination of TPD and FT-RAIRS, we can constrain the evolution of the different molecules involved in the CO + H reactive systems. The quantity of products observed (or not) in addition to the condition used are summarized in Table 1.

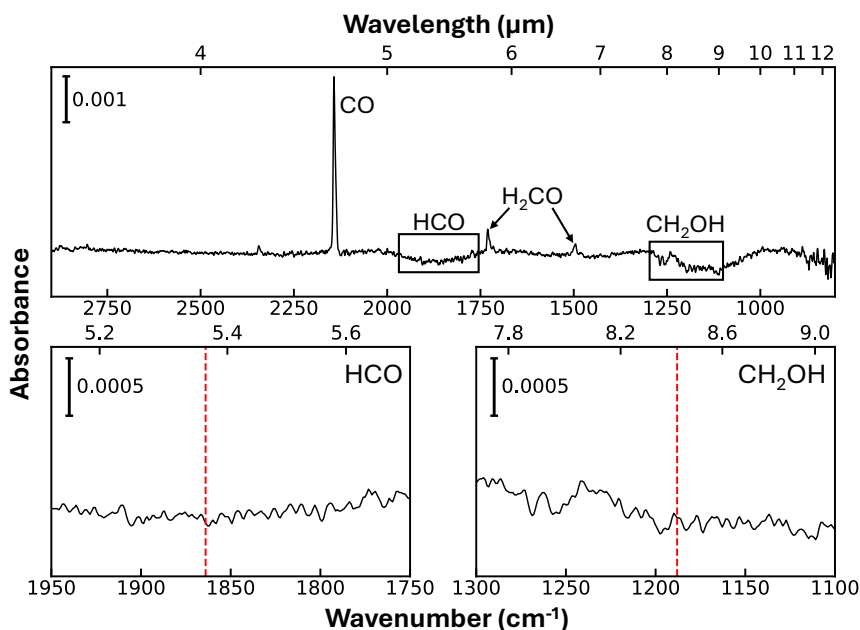


Figure 5: The infrared absorption spectra from the CO+H co-deposition experiment (experiment #4 from table 1). The top panel shows the global spectra, identifying CO at 2140 cm^{-1} and H_2CO at 1730 cm^{-1} and 1494 cm^{-1} , while CH_3OH remains undetected due to its low abundance. The lower panel focuses on HCO radical at 1864 cm^{-1} and CH_2OH at 1188 cm^{-1} ,⁵⁷ which are not detected in our experiments.

Rate-equations approach

There are different theoretical methods for studying the chemical evolution of ice and molecules on the surface of ice, such as quantum calculations, Kinetic Monte Carlo calculations and classical rate equation approaches.⁵⁸ In the scope of this project we decided to base our theoretical studies on the Rate Equation (RE) approach and use astrochemical codes that utilize this approach: MONACO,⁵⁹ NAUTILUS¹³ and pyRate.¹²

The RE approach is the standard method for modelling complex gas-dust chemistry (e.g., Vasyunin et al.⁹, Ruaud et al.¹³, Hasegawa et al.⁶⁰, Hasegawa and Herbst⁶¹, Garrod et al.⁶²). This type of code takes into account the rates and probabilities of accretion of atoms and molecules on dust particle surfaces, their migration on the dust surface, the probabilities of molecule formation, and the probabilities of the molecule desorption to the gas phase. All codes used in this paper can calculate the gas-phase chemistry and chemistry on the dust surfaces with different conditions of the environment and different hypotheses.

The kinetic equations for the gas-phase species that are used in this method have the general form:

$$\frac{dn_{i,gas}}{dt} = \sum_{j,k} k_{j,k} n_j n_k + \sum_l k_l n_l - n_i \left[\sum_m k_{im} n_m + \sum_n k_n \right] + k_{des} n_{i,s} - k_{acc} n_i, \quad (3)$$

where n_i — abundance of i-th compound that we need to know; $k_{j,k}$ and k_l , k_{im} and k_n , k_{des} , k_{acc} — the rate coefficients of the reactions of formation (first pair), molecule destruction (second pair), desorption, and accretion, respectively. For the equations of chemical kinetics on the dust surface, the signs (+ or -) of the $k_{des} n_{i,s}$ and $k_{acc} n_i$ are reversed:

$$\frac{dn_i}{dt} = \sum_{j,k} k_{j,k} n_j n_k + \sum_l k_l n_l - n_i \left[\sum_m k_{im} n_m + \sum_n k_n \right] - k_{des} n_{i,s} + k_{acc} n_i. \quad (4)$$

Despite the advantages of this approach (ease of use, relatively fast calculations), there are also disadvantages that can be ignored in the present study. For example, the RE method is a

macroscopic approach that does not take into account all microscopic details on the dust surface and can not track the position of atoms and molecules on the surface of dust. It can lead to the overproduction of some molecules, as soon as method operates with the averaged values of the species (it is especially important when the number of species on the dust surfaces is low).⁶³ For now, our main goal is to try to show that data from astrochemical codes based on the RE approach can be used for comparison with laboratory results: they can reproduce results that we see with simple experiments (with a given level of uncertainties) and later can be used for prediction of products that can be possibly found in experiments.

Below we describe what was adapted in the codes to mimic laboratory experiments. In principle, we did not change the codes in technical terms (functions, used packages, additional parts of the code), or physical terms (such as adding or removing a process), but changed only the input parameters. For all codes general rules were:

1. Gas phase interactions are neglected: all gas phase reactions are turned off, except for the freeze-out of species from gas phase to the surface of dust;
2. Only thermal and chemical desorption are allowed in all codes;
3. In all codes we use the same parameters for grains: each grain is assumed to be a uniform spherical particle with a radius of $0.1\text{ }\mu\text{m}$, and its number density is calculated using the gas to dust ratio of 1%;
4. The surface of dust particles is assumed to be compact with density of $1.5\times 10^{15}\text{ sites cm}^{-2}$ (or about 10^6 sites per grain). Grain material density is set to 3 g/cm^3 . These are the standard parameters for all the codes, and they were not changed in the present study;^{9,12,13,64}
5. Gas-phase chemistry and chemistry on the dust surfaces are connected via accretion and desorption processes, sticking probability is set to 1 in the case of MONACO (for most molecules, except for H and H₂, for them sticking coefficients are calculated separately) and NAUTILUS codes. In the case of pyRate, the sticking coefficient of H is computed following

the Cuppen equations,⁶⁵ with probabilities of 0.42 at a gas temperature of 293 K and a dust temperature of 10 K. For H₂ and CO, the sticking coefficients are derived using the He equations,⁶⁶ yielding sticking probabilities of 0.62 and 1.0, respectively. All other molecules are assumed to have a sticking probability of 1. For all codes, the species accreted from the gas phase can react through the Eley-Rideal mechanism with species on the surface, or diffuse via thermal hopping. In case of H and H₂, diffusion by thermal hopping or tunnelling was considered.

6. Binding-to-diffusion energy ratios are different from one code to another. For MONACO code $E_d / E_b = 0.5$ for the surface (and 1.0 for the bulk), for NAUTILUS - 0.4 (and 0.8 for the bulk) and for pyRate - 0.55 (with no diffusion for the bulk).

MONACO code and results

MONACO code is a gas-grain chemical model based on the RE approach for treating gas-phase reactions⁵⁹ and modified RE approach for reactions inside the ice bulk.^{67,68} This code implements a multi-phase approach for studying the chemical evolution of species: gas-phase chemistry, chemistry on the surface and chemistry inside the interstellar ice. Kinetic equations for chemistry on the grain surfaces take into account the complex structure of ice mantles, which consists of the bulk phase and ice surface, migration of species inside the ice, and much more. The detailed description of the 3-phase treatment of chemistry can be found in Vasyunin et al.⁹.

The MONACO code operates with relative abundances of species. To calculate the number of molecular monolayers on the dust surface we need to recalculate these abundances using the assumption:

$$N_{ML} = X \cdot \frac{n}{n_{dust} \cdot N_{sites}}, \quad (5)$$

where X is the relative abundance of the molecule $n(X)/n_H$ (here n_H is the total abundance of hydrogen equal $n(H) + 2n(H_2)$), n - number density of gas in the system, n_{dust} - number density

of dust grains in the system, N_{sites} - number of sites on the surface. For the proper calculation of $n(X)$, we need to take into account species in the bulk and on the ice surface as a sum. Here and after we will denote all the molecules as follows: X (if species do not have a prefix) as a molecule in the gas phase, gX — molecule on the grain surface, mX — molecules from bulk and surface together (gX + bX).

In the MONACO code we use the KIDA database,^{26,27} which takes into account not only gas-phase reactions but also reactions on the surface of dust particles and their ice mantles. The main reactions leading to the formation of methanol (and important in {CO+H} system) are presented in Table 2.

Experiment #1 and #2: CO deposition on the surface and CO+H co-deposition with reference fluxes

We started our calculation tests with simple CO deposition on the grain surface following the protocol of experiments described before. The main physical parameters that we need to know and put into the system are the gas and dust temperatures (T_{gas} and T_d , respectively), the gas abundance ($n(H)$) and the initial abundance of CO. All other parameters will remain untouched.

The CO gas-phase abundance is derived using the standard formula of accretion, assuming that the flux that we see in the laboratory is indeed our accretion rate:

$$k_{acc} = n \sigma_d v S(T_{gas}, T_d), \quad (6)$$

where n — the number density of particles in the gas in cm^{-3} ; σ_d — the effective cross-section of the dust grains, close to its geometric area in cm^2 ; v — the average thermal velocity of the gas particles in cm/s ; S — the sticking coefficient, dimensionless. In the case of CO deposition for our tests, we have: $S(T, T_d)$ equals to unity (all particles stick to the surface), $T_{gas} = 300 \text{ K}$, $T_d = 10 \text{ K}$, and $k_{acc(CO)} = 1.67 \times 10^{12} \text{ molecules cm}^{-2} \text{s}^{-1}$, from our experimental conditions. Hence, the

number density of CO in the gas phase can be calculated as follows:

$$n(CO) = \frac{1.67 \times 10^{12} \text{ molecules cm}^{-2} \text{s}^{-1}}{\pi \cdot a_{gr}^2 \cdot v} = 1.15 \times 10^8 \text{ cm}^{-3}. \quad (7)$$

All of that leads us to the first model with given parameters:

1. $n = 1.15 \times 10^8 \text{ cm}^{-3}$ - as gas number density (n_H);
2. $T_{gas} = 300 \text{ K}$, $T_d = 10 \text{ K}$;
3. initial gas-phase abundance: $n(CO)/n_H = 1$.

Figure 6 shows results for modelling CO deposition on the surface of a dust grain: growth of the CO ice and saturation of the chemical layer which is equal to 1 ML. These results fit great with experimental data and give us 1.1 ML of CO ice in 10 minutes.

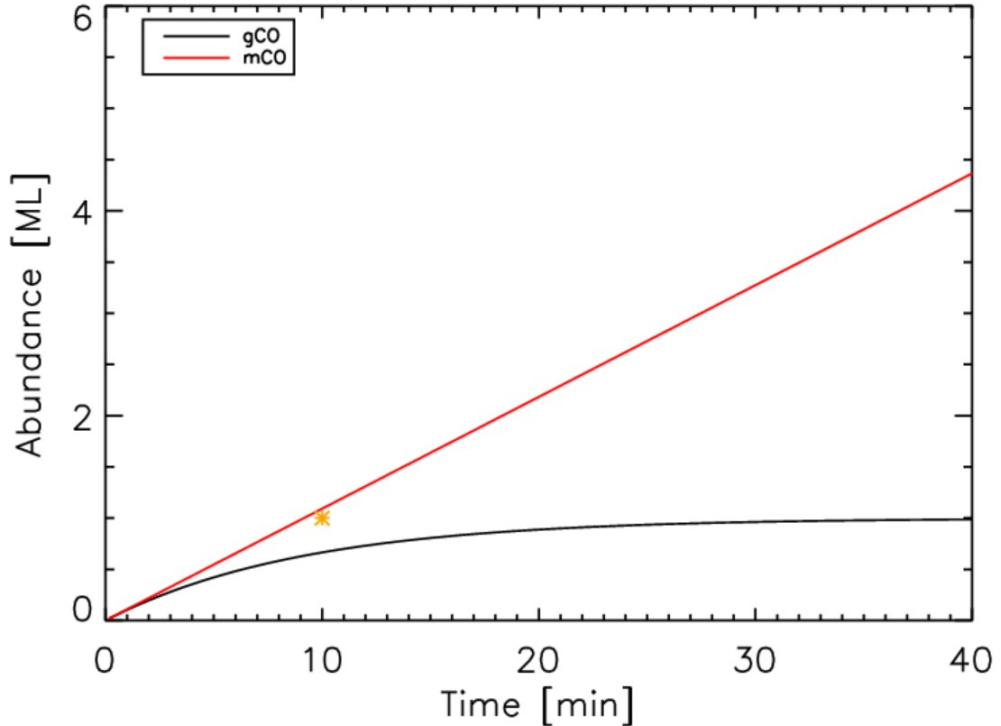


Figure 6: Experiment #1: Growth of the CO ice on the surface, MONACO code. mCO denotes molecules from bulk and surface together (red line). Saturation of the chemical layer (black line), where the active layer is set to be equal to 1. The orange star represents results from the experiments, where we obtain 1 ML of CO on the surface in 10 minutes.

After that, we added the hydrogen flux to our system, taking into account values that were given in the Table 1 for Experiment #2. Hence, the number density of H in the system will be:

$$n(H) = \frac{6.67 \times 10^{12} \text{molecules cm}^{-2}\text{s}^{-1}}{\pi \cdot a_{gr}^2 \cdot v \cdot 0.8} = 1.07 \times 10^8 \text{ cm}^{-3}, \quad (8)$$

where 0.8 is the sticking coefficient of H (calculated in the code,⁹ using a formula from Hollenbach and McKee⁶⁹).

All of that gives us the following set of parameters:

1. $n = 1.074 \times 10^8 \text{ cm}^{-3}$ - as gas number density (n_H);
2. $T_{gas} = 300 \text{ K}$, $T_d = 10 \text{ K}$;
3. initial gas-phase abundances: $n(H)/n_H = 1$, $n(CO)/n_H = 1.07$. It is important to note that one must carefully recalculate this parameter every time the density changes;
4. models were calculated in two regimes: tunnelling of light species (H) is turned on and off;
5. methanol-production reaction chain, that presented in Table 2, is used for calculating the chemistry.

Table 3 displays the result of modelling for Experiment #2 with two regimes: with tunnelling of light species (H) on and off. As can be seen from the results, if tunnelling diffusion for light species is turned on, all hydrogen atoms quickly transform into molecular hydrogen and almost no {CO+H} chemistry occurs on the surface of dust particles. According to Senevirathne et al.⁷⁰, tunnelling of H atoms plays a significant role in the chemistry of H₂ on the surface of ASW with temperatures around 10 K and lower. In addition to that, they mention that all their calculation results for binding energies and rate constants are strongly dependent on the morphology and structure of the surface. In our models, the dust grain and the ice surface are uniform, so we suggested that $T_{dust}=10 \text{ K}$ could be too high for the tunnelling to dominate over thermal hopping. Indeed, the so-called crossover temperature T_c at which the tunnelling effect is similar to the thermal crossing

Table 2: Table of reactions included in the methanol-formation chain. Here, E is the energy of the process (binding energy or activation energy depending on the type of the process) in each of the codes: E_{MC} , E_{NT} , E_{PR} for energies in MONACO, NAUTILUS and pyRate codes, respectively. x denotes reactions that are not included in the code's chemical network.

| Reaction | E_{MC} | E_{NT} | E_{PR} |
|---|----------|----------|----------|
| $\text{CO} \rightarrow \text{gCO}^a$ | 0.0 | 0.0 | 0.0 |
| $\text{H} \rightarrow \text{gH}^a$ | 0.0 | 0.0 | 0.0 |
| $\text{H}_2 \rightarrow \text{gH}_2^a$ | 0.0 | 0.0 | 0.0 |
| $\text{gCO} \rightarrow \text{CO}^b$ | 1322.0 | 1300.0 | 1150.0 |
| $\text{gHCO} \rightarrow \text{HCO}^b$ | 1600.0 | 2400.0 | 1600.0 |
| $\text{gH}_2\text{CO} \rightarrow \text{H}_2\text{CO}^b$ | 4009.0 | 4500.0 | 2050.0 |
| $\text{gCH}_3\text{O} \rightarrow \text{CH}_3\text{O}^b$ | 4400.0 | 4400.0 | 3800.0 |
| $\text{gCH}_2\text{OH} \rightarrow \text{CH}_2\text{OH}^b$ | 5080.0 | 4400.0 | 5084.0 |
| $\text{gCH}_3\text{OH} \rightarrow \text{CH}_3\text{OH}^b$ | 5740.0 | 5000.0 | 5534.0 |
| $\text{gH} \rightarrow \text{H}^b$ | 450.0 | 650.0 | 450.0 |
| $\text{gH}_2 \rightarrow \text{H}_2^b$ | 430.0 | 440.0 | 500.0 |
| $\text{gH} + \text{gH} \rightarrow \text{gH}_2$ | 0.0 | 0.0 | 0.0 |
| $\text{gH} + \text{gCO} \rightarrow \text{gHCO}$ | 2320.0 | 2500.0 | 1730.0 |
| $\text{gH} + \text{gHCO} \rightarrow \text{gH}_2\text{CO}$ | 0.0 | 0.0 | 0.0 |
| $\text{gH} + \text{gHCO} \rightarrow \text{gCO} + \text{gH}_2$ | 0.0 | x | 0.0 |
| $\text{gH} + \text{gH}_2\text{CO} \rightarrow \text{gHCO} + \text{gH}_2$ | 2960.0 | 1740.0 | 3000.0 |
| $\text{gH} + \text{gH}_2\text{CO} \rightarrow \text{gCH}_2\text{OH}$ | 4500.0 | 5400.0 | 5160.0 |
| $\text{gH} + \text{gH}_2\text{CO} \rightarrow \text{gCH}_3\text{O}$ | 2320.0 | 2200.0 | 2000.0 |
| $\text{gH} + \text{gCH}_2\text{OH} \rightarrow \text{gCH}_3\text{OH}$ | 0.0 | 0.0 | 0.0 |
| $\text{gH} + \text{gCH}_3\text{O} \rightarrow \text{gCH}_3\text{OH}$ | 0.0 | 0.0 | 0.0 |
| $\text{gH} + \text{gCH}_2\text{OH} \rightarrow \text{gH}_2\text{CO} + \text{gH}_2$ | 0.0 | x | 0.0 |
| $\text{gH} + \text{gCH}_3\text{O} \rightarrow \text{gH}_2\text{CO} + \text{gH}_2$ | 0.0 | x | 0.0 |
| $\text{gH} + \text{gCH}_3\text{OH} \rightarrow \text{gCH}_2\text{OH} + \text{gH}_2$ | 4380.0 | 2600.0 | 3620.0 |
| $\text{gH} + \text{gCH}_3\text{OH} \rightarrow \text{gCH}_3\text{O} + \text{gH}_2$ | 6640.0 | 4000.0 | 5560.0 |

^aFreeze-out on the surface; ^bDesorption from the surface

has been calculated to be lower than 10 K in the case of H diffusion on amorphous solid water ice.⁷¹ As one can see, for our experiments the thermal hopping of hydrogen seems to be a better description than tunnelling, even though the substrate is not amorphous solid water ice but a gold surface (not monocrystalline).

Table 3: Modelling results from MONACO code for Experiment #2 with two regimes: tunnelling of light species on and off. Monolayers are calculated for the sum of bulk and surface quantities of molecules.

| | CO | HCO | H ₂ CO | CH ₂ OH (ML) | CH ₃ O | CH ₃ OH |
|---|-------|-----------|-------------------|----------------------------|-------------------|--------------------|
| Experimental results (from Table 1) | 0.730 | - | 0.11 | - | - | 0.097 |
| <hr/> | | | | | | |
| Modelling results | | | | | | |
| Tunneling diffusion of light species on | 1.664 | 3.217(-9) | 2.141(-3) | 3.885(-15) | 4.590(-12) | 2.740(-6) |
| Tunneling diffusion of light species off | 0.982 | 1.400(-3) | 0.298 | 1.224(-4) | 4.098(-4) | 0.139 |

One of the possible solutions for controlling the molecule production here is the variation of the H-atom flux in the system. Figure 7 shows how the H-flux variation in the case of Experiment #2 influences the chemical composition of dust ices. Calculations show that the higher we take the flux - the stronger the destruction of CO, and in most cases we see the overproduction of H₂CO and CH₃OH in comparison with experiments.

In general, modelling results for Experiments #1 and #2 are close to the ones that we see in the laboratory, even though the production effectiveness of all molecules appears to be a little higher than in the experiments. Indeed, the missing part is underestimated, indicating that the chemical desorption is possibly also undervalued.

Experiments #4-#8: CO deposition and CO+H co-deposition

We do not show the results from modelling of the Experiment #3 here because in principle they are the same as the results for Experiment #2: the growth of mCO follows the same linear trend and gives us 7.2 ML of CO in 60 minutes. In the set of experiments (#4-#8) we studied the co-

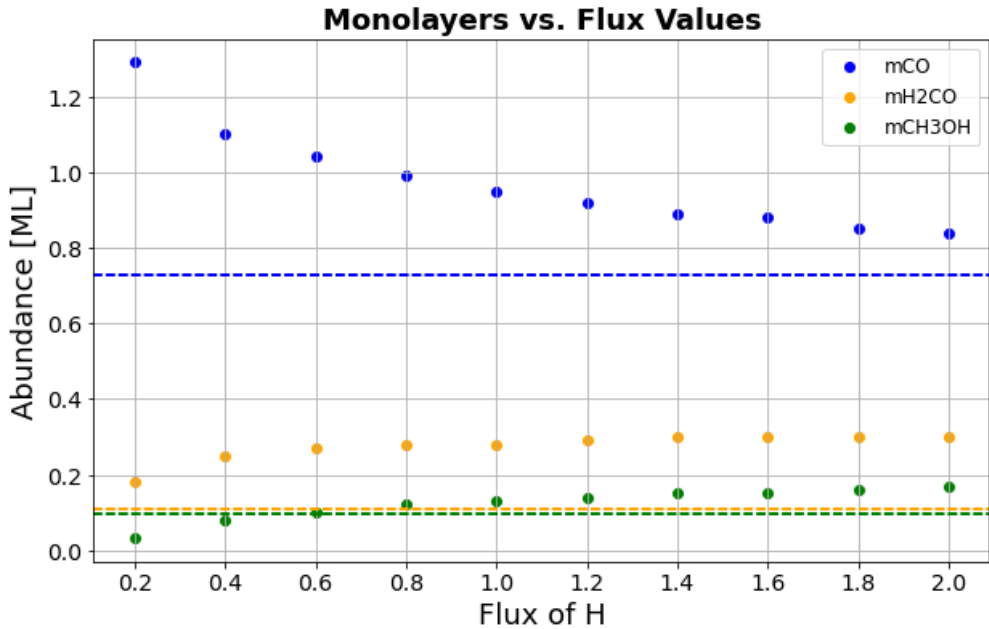


Figure 7: H-atom flux variation vs number of monolayers for CO, H₂CO and CH₃OH. Dashed lines represent the laboratory results for each molecule, dots note the amount of monolayers for each molecule. The base H-atom flux was taken as $n = 1.074 \times 10^8 \text{ cm}^{-3}$ (corresponds to 1.0 on the X axis of the graph)

deposition {CO+H} with different temperatures of the surface (from 9 to 15 K).

Using the same Equation 6 we derived new abundances for H atoms and CO molecules in the system, using new laboratory fluxes from Table 1: $n(H) = 5.3 \times 10^7 \text{ cm}^{-3}$, $n(CO) = 1.26 \times 10^8 \text{ cm}^{-3}$.

Here, we started our calculating with Experiment #5 hence deposition at 10 K is considered to be standard for the experiments. Figure 8 shows results for modelling co-deposition of CO and H for the system with the following parameters:

1. $n = 5.3 \times 10^7 \text{ cm}^{-3}$ - as gas number density (n_H);
2. $T_{gas} = 300 \text{ K}$, $T_d = 10 \text{ K}$;
3. initial gas-phase abundances: $n(H)/n_H = 1$, $n(CO)/n_H = 2.38$;
4. methanol-production reaction chain, that presented in Table 2.

From modelling results we see the overproduction of CO, H₂CO, and CH₃OH molecules. In our study we use the same treatment of reactive desorption, noted RD, that is used in Vasyunin et al.⁹.

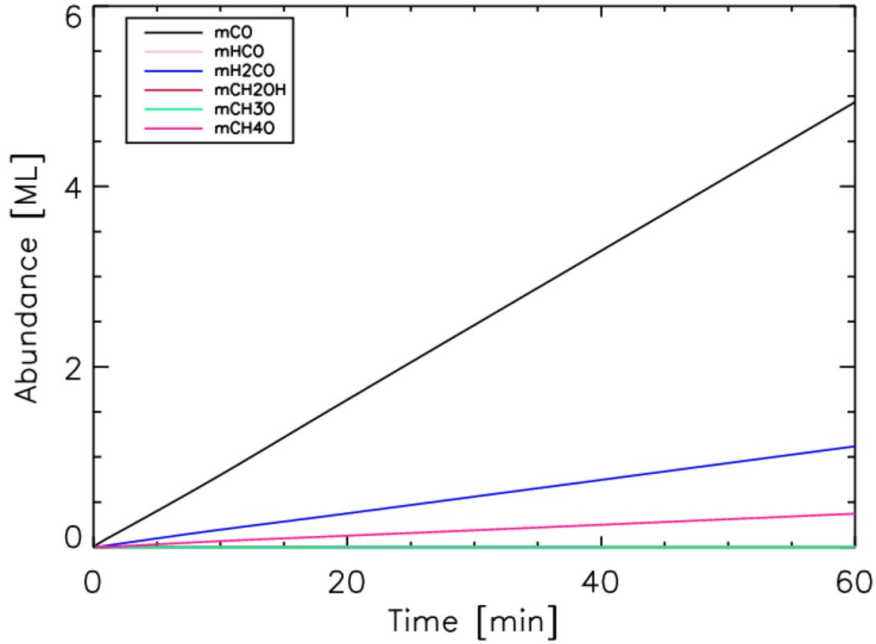


Figure 8: Modelling results for Experiment #5 (co-deposition of CO and H - {CO+H} - at surface temperature of 10 K), the MONACO code. mX (where X is the chemical formula of the compound) denotes molecules from bulk and surface together.

In this work they implemented the results from experiments of Minissale et al.⁷² and described the dependence of the RD efficiency (R_{RD}) on important surface parameters (the composition of the surface, surface reaction exothermicity, and binding energies of reaction products):

$$R_{RD} = \exp\left(-\epsilon \frac{E_b \times DF}{\Delta H}\right), \quad (9)$$

where E_b is the binding energy, DF is the number of vibrational modes in the molecule–surface bond system, and ϵ is the fraction of kinetic energy kept by the reaction product.

In their study, Vasyunin et al.⁹ show the same problem with overproduction of H_2CO and CH_3OH on the surface of dust particles in comparison with observations of interstellar ices, referring to the semi-empirical nature of expression for RD that was based on the limited set of experiments (in addition, the same issue was discussed in Punanova et al.⁷³). Moreover, some parameters that this expression uses are arguable: for example, the binding energies of certain molecules are still unknown, which also requires the revision of the parameters of the chemical

network used in the code and leads to the extrapolation of results from well-known systems to poorly known ones. Thus, one of the possible explanations for the overproduction of H₂CO and CH₃OH that we see in our results is the insufficiently accurate treatment of RD for these species and their reaction systems.

One way to get more precise results would be the changing of the binding energy of H atoms to control the hydrogenation rate of all reactants and activation energy of the reaction CO + H → HCO, the key step in the H₂CO production reaction chain. The activation energy (E_a) of reactions is one of the crucial issues in laboratory and theoretical astrochemistry. CO + H → HCO reaction was well studied by several groups, and E_a values for this reaction vary from 1635 K⁷⁴ to 2320 K.⁷⁵ The same uncertainties come for the binding energy of hydrogen: in the chemical network that we used in past models and studies it is assumed that $E_b(\text{H}) = 450$ K (from the OSU gas-grain code of Eric Herbst group in 2006, where it was calculated in Hasegawa et al.⁶⁰), but in recent experiments the value 661 K was introduced (Senevirathne et al.⁷⁰). This parameter directly affects the key chemical parameter, the diffusion energy E_d (see the discussion in Ligterink et al.⁷⁶) via the $E_d = \beta E_b$ relation. In the case of MONACO code, $\beta = 0.5$.

In our study, we decided to vary both values ($E_b(\text{H})$ and $E_a(\text{CO}+\text{H})$) and see how it affects the modelling results: for hydrogen diffusion estimation, we took values in the range 350 K < $E_b(\text{H})$ < 650 K, for the CO+H reaction, we considered 1700 K < $E_a(\text{CO}+\text{H})$ < 2900 K. The first parameter probes the H diffusion while the second affects the H reactivity with CO.

Figure 9 shows the agreement maps for the calculation grid, where we varied $E_b(\text{H})$ and $E_a(\text{CO}+\text{H})$. We calculated the agreement between laboratory and modelling results using the Residual sum of squares (RSS) approach. In this approach, we calculated the total squared difference for each combination of parameters:

$$\text{RSS} = \sum_{i=1}^n (\text{Model Abundance}_i - \text{Laboratory Abundance}_i)^2, \quad (10)$$

where n is the number of molecules considered for the comparison. Lower values of this sum

indicate that the modelling results better fit with the laboratory measurements, while higher values indicate that the model results deviate significantly from laboratory data.

Based on the RSS approach, we derived the best-fit points, i.e. the set of parameters that show the best agreement between results. The top panel in Figure 9 shows the agreement map and best-fit points if RSS is calculated for all 3 molecules. The value of CO gives the largest contribution to the RSS values, thus we decided to build the additional map only for H₂CO and CH₃OH (bottom panel in Figure 9).

Analysis of both best-fit results shows that there is no set of parameters which provides good agreement for all three molecules at once: either we have a high value for CO, or the overproduction of H₂CO and CH₃OH. Another constraint set by results from the table 1 is that there are no signs of HCO or CH₃O in Experiment #5 both on TPD or IR spectra. Based on this, $E_b(H) \geq 550$ K are not considered as with these values, we measure large amounts of HCO or CH₃O - around 0.4 and 0.2 ML respectively, which is not matching the laboratory results. On the other hand, $E_b(H) < 400$ K appears to be very low and can lead to high overproduction of CO with larger $E_a(CO+H)$ (values closer to 2900 K) and high overproduction of H₂CO with lower $E_a(CO+H)$ ((values closer to 1700 K). In addition to that, from the agreement maps we note that there is an intersection between good fitting areas when $2320 \text{ K} \leq E_a(CO+H) \leq 2550$ K. Therefore, we arrive at the following ranges: $2320 \text{ K} \leq E_a(CO+H) \leq 2550$ K and $400 \text{ K} \leq E_b(H) \leq 500$ K.

From these values, we choose the point with the lowest RSS: $E_b(H) = 500$ K and $E_a(CO+H) = 2320$ K, where RSS = 1.43 (see Table 4). These energy values are consistent with values obtained by other groups. For example, Borshcheva et al.⁷⁷ calculated $E_b(H) = 480$ K based on the work of Minissale et al.⁷⁸, and $E_a(CO+H) = 2320$ K. For further analysis, we keep these two values fixed ($E_b(H) = 500$ K and $E_a(CO+H) = 2320$ K).

In the next step, in an attempt to improve the agreement between experimental and model results, the following parameters have been changed (the initial parameters for these reactions are shown in Table 2):

1. the branching ratios for reactions H + HCO → H₂CO and H + HCO → CO + H from 0.5 each

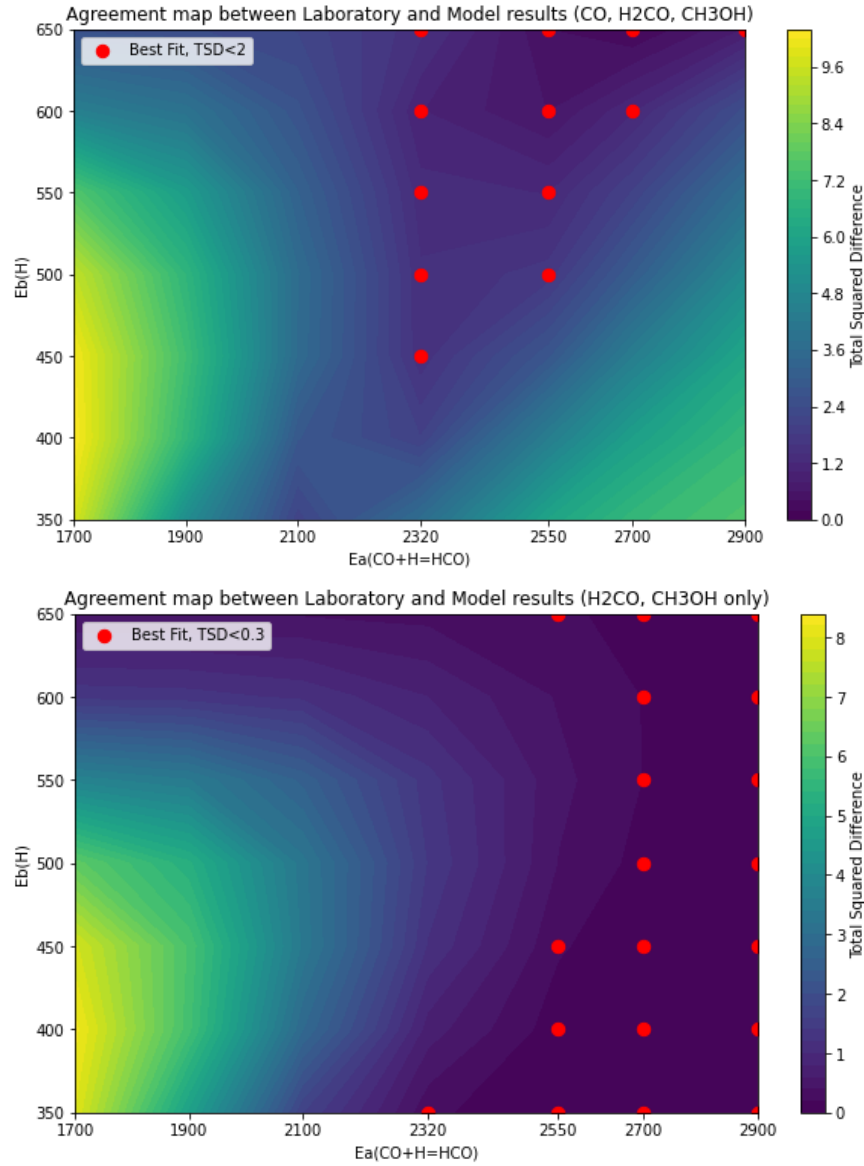


Figure 9: Agreement map between laboratory and modelling results in the case of the MONACO code, Experiment #5 (co-deposition {CO+H} with $T_{surf} = 10$ K). Red dots denote the best-fit pair of parameters, where in the upper panel, RSS is calculated for all 3 molecular abundances and is lower than 2.0; in the bottom panel, RSS is calculated only for H₂CO and CH₃OH and is lower than 0.3

to 0.33 and 0.67, respectively (according to Ioppolo et al.⁷⁹), in order to vary the amount of H₂CO and CO;

2. E_a of H₂CO + H → HCO + H₂ reaction from 2960 to 2470 K, to slow down the H₂CO production;

Table 4: Modelling results from the MONACO code for Experiment #5 (co-deposition {CO+H} with $T_{surf} = 10$ K): chemical composition of the ice before modifications in the initial chemical network, at the "best fit point" ($E_b(\text{H}) = 500$ K and $E_a(\text{CO+H}) = 2320$ K), and after modifications in the chemical network at the "best fit" point. Monolayers are calculated summing bulk and surface molecules.

| | CO | HCO | H_2CO | CH_2OH | CH_3O | CH_3OH |
|-------------------------------------|-------|-----------|-----------------------|------------------------|-----------------------|------------------------|
| | (ML) | | | | | |
| Experimental results | 4.478 | - | 0.105 | - | - | 0.031 |
| Modelling results | | | | | | |
| Before modifications | 5.005 | 6.708(-3) | 1.134 | 3.323(-4) | 1.521(-3) | 0.376 |
| "Best fit" point | 4.699 | 4.092(-2) | 1.202 | 2.354(-3) | 9.864(-3) | 0.454 |
| "Best fit" point with modifications | 5.545 | 3.900(-2) | 0.306 | 1.454(-3) | 2.035(-3) | 3.242(-2) |

3. E_a of $\text{CH}_3\text{OH} + \text{H} \rightarrow \text{CH}_3\text{O} + \text{H}_2$ and $\text{CH}_3\text{OH} + \text{H} \rightarrow \text{CH}_2\text{OH} + \text{H}_2$ from 6640 to 5530 K and from 4380 to 3610 K, respectively (according to Qasim et al.⁷⁴), to regulate methanol destruction.

All these changes give us an agreement between laboratory and modelling values with RSS = 1.16, where the highest impact comes from the CO abundance. Considering the uncertainties associated with chemical desorption, this set gives us the best agreement between experimental and model results.

Taking into account all the changes described above, we performed calculations for Experiments #4-#8, where the surface temperature was changed. Table 5 shows the modelling results for all 5 molecules on the dust surface: CO, HCO, H_2CO , CH_3O and CH_3OH . The difference in abundances between models is not as high as in the case of laboratory experiments. However, modelling results are still in good agreement with them. In experiments with $T_{dust} = 15$ K we have RSS = 0.2, which indicates a great agreement between the results.

Experiments #9-#10: CO+H experiments

In this section, we show the results of modelling for experiments where the pre-deposited CO ice is hydrogenated. Figure 10 shows the results of the modelling with the following initial parameters:

1. $n = 5.3 \times 10^7 \text{ cm}^{-3}$ - as gas number density (n_H);

Table 5: Laboratory results (from Table 1 and results of simulations with the MONACO code for $\{\text{CO} + \text{H}\}$ 60 min deposition $\{\text{CO} + \text{H}\}$ with different surface temperatures (Experiments #4-#8)

| Experiment | T_{surf} (K) | CO | HCO | H_2CO | CH_2OH (ML) | CH_3O | CH_3OH |
|---------------------------|--------------------------|-------|-----------|-----------------------|--------------------------------|-----------------------|------------------------|
| Laboratory results | | | | | | | |
| #4 | 9 | 4.063 | - | 0.169 | - | - | 0.039 |
| #5 | 10 | 4.478 | - | 0.105 | - | - | 0.031 |
| #6 | 11 | 5.948 | - | 0.053 | - | - | 0.021 |
| #7 | 12 | 6.448 | - | 0.036 | - | - | 0.015 |
| #8 | 15 | 6.593 | - | 0.018 | - | - | 0.010 |
| Modelling results | | | | | | | |
| #4 | 9 | 5.437 | 1.260(-1) | 3.164(-1) | 4.796(-3) | 1.006(-2) | 3.758(-2) |
| #5 | 10 | 5.545 | 3.900(-2) | 3.065(-1) | 1.454(-3) | 2.035(-3) | 3.242(-2) |
| #6 | 11 | 5.591 | 2.134(-2) | 3.050(-1) | 7.243(-4) | 9.834(-4) | 3.137(-2) |
| #7 | 12 | 5.64 | 1.363(-2) | 3.054(-1) | 4.524(-4) | 6.206(-4) | 3.102(-2) |
| #8 | 15 | 6.125 | 9.528(-4) | 2.894(-1) | 2.286(-5) | 3.926(-5) | 2.546(-2) |

2. $T_{\text{gas}} = 300$ K, $T_d = 9$ K (see Experiments #8 -#9 in Table 1);
3. initial abundances: $n(\text{H})/n_H = 1$, $n(\text{gCO})/n_H = 8.53 \times 10^{-7}$; $n(\text{bCO})/n_H = 6.42 \times 10^{-7}$, where abundances for gCO and bCO are taken from the modelling CO-only deposition for 9 minutes (according to the time of Experiments #8 -#9 at the Table 1);
4. two chemical networks: the one described above with the best-fit $E_a(\text{CO} + \text{H})$ and $E_b(\text{H})$ values, and the standard one from Table 2, where only $E_b(\text{H}) = 500$ K is changed.

We note a non-monotonic and non-linear behaviour of CO in the first minutes (shown in both panels of Figure 10) as a result of the HCO destruction and transition back to CO. This raises the problem with IR detection of radicals (HCO, CH_3O or CH_2OH) that have never been detected during our experiments. For comparison, the decrease in the IR signal of CO is quite linear (without fast increases/decreases as seen in the bottom panel of Figure 10), and both H_2CO and CH_3OH are detectable. Thus, while modifying diffusion and reactivity barriers and adapting branching ratios can significantly improve results, there are still issues to be addressed, especially the too high accumulation of radicals predicted by the model.

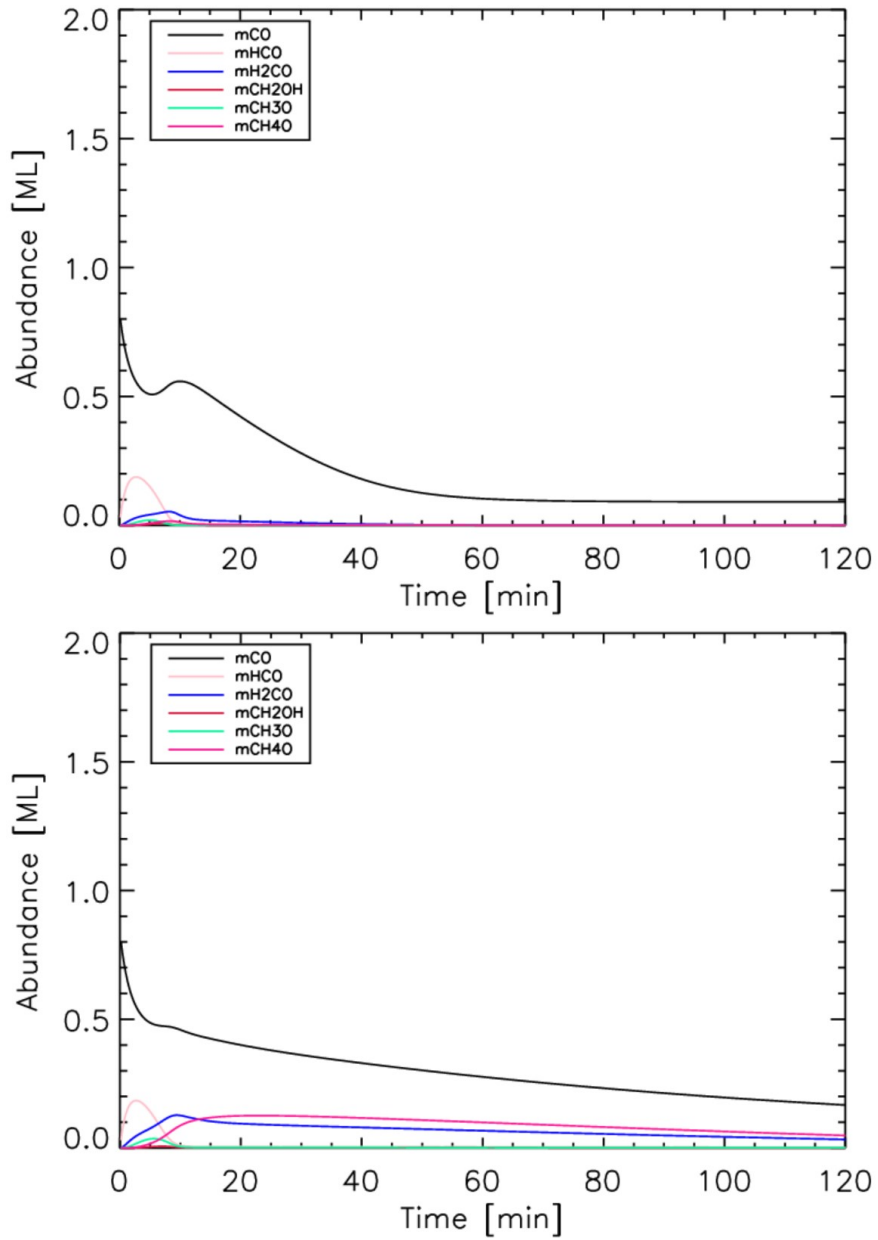


Figure 10: Modelling results for deposition of CO followed by deposition of H (Experiment #9 with hydrogenation time of 120 min and #10 with hydrogenation time of 75 min) with best-fit network (on the top) and standard network (on the bottom). mX (where X is the chemical formula of the compound) denotes molecules from bulk and surface together.

NAUTILUS code and results

Nautilus is a public astrochemical code that calculates chemical abundances (in gas-phase and on interstellar grain surfaces) as a function of time for given physical conditions. First presented

in Ruaud et al.¹³, this three-phase code can calculate not only the gas chemistry but also the chemistry of surface species in the outer monolayers (2 in the case of the present research) and the bulk mantle underneath.

The calculation of the chemical evolution of species is based on the rate equation method described above (Section Rate-equations approach,⁶¹). The competition between diffusion, desorption, and reaction (as discussed by Chang et al.⁸⁰ and Garrod and Pauly⁸¹) is included in the model. In more detail, the NAUTILUS code is described in Ruaud et al.¹³. All model parameters are explicitly provided in the code and can be adjusted for specific applications.

We decided to calibrate fluxes and find the monolayer conversion coefficient using a mixture of H₂ and CO together, since these two molecules do not react. The reason for this choice is that the abundances are given in relative values to H, and we have retained this approach to avoid potential numerical problems. Figure 11 represents the CO deposition of one ML in 10 minutes to mimic experiments listed in Table 1. Here, we found that with $n(H) = 2.1 \times 10^9 \text{ cm}^{-3}$ the modelling results match the results of Experiment #1 and give 1 ML of CO ice in 10 minutes (see Fig. 11 for the linear growth of the CO monolayer and for the layer saturation). We observe a slightly different behaviour of the shape of the saturation curve of surface species compared to Figure 6 using the MONACO code. This is not only due to the thickness of the chemical layer (2 vs. 1), but may also shed light on the different treatments of the surface to bulk conversion.

Table 6: Results of simulations with the NAUTILUS code for {CO + H} 60 min deposition with different surface temperatures (Experiments #4-#8). Tunnelling of H diffusion is turned on; diffusion barrier thickness is $2.5 \times 10^{-8} \text{ cm}$.

| Experiment | T (K) | CO | HCO | H ₂ CO | CH ₂ OH (ML) | CH ₃ O | CH ₃ OH |
|------------|----------|-------|-------|-------------------|----------------------------|-------------------|--------------------|
| #4 | 9 | 5.089 | 0.124 | 1.034 | 0.001 | 0.011 | 0.309 |
| #5 | 10 | 5.089 | 0.124 | 1.034 | 0.001 | 0.011 | 0.309 |
| #6 | 11 | 5.089 | 0.124 | 1.034 | 0.001 | 0.011 | 0.309 |
| #7 | 12 | 5.089 | 0.124 | 1.034 | 0.030 | 0.011 | 0.309 |
| #8 | 15 | 5.098 | 0.118 | 1.033 | 0.001 | 0.010 | 0.307 |

Following the same scenario for MONACO and pyRate codes, we have simulated the different experiments one after another, starting with Experiment #4. Table 6 shows the results obtained

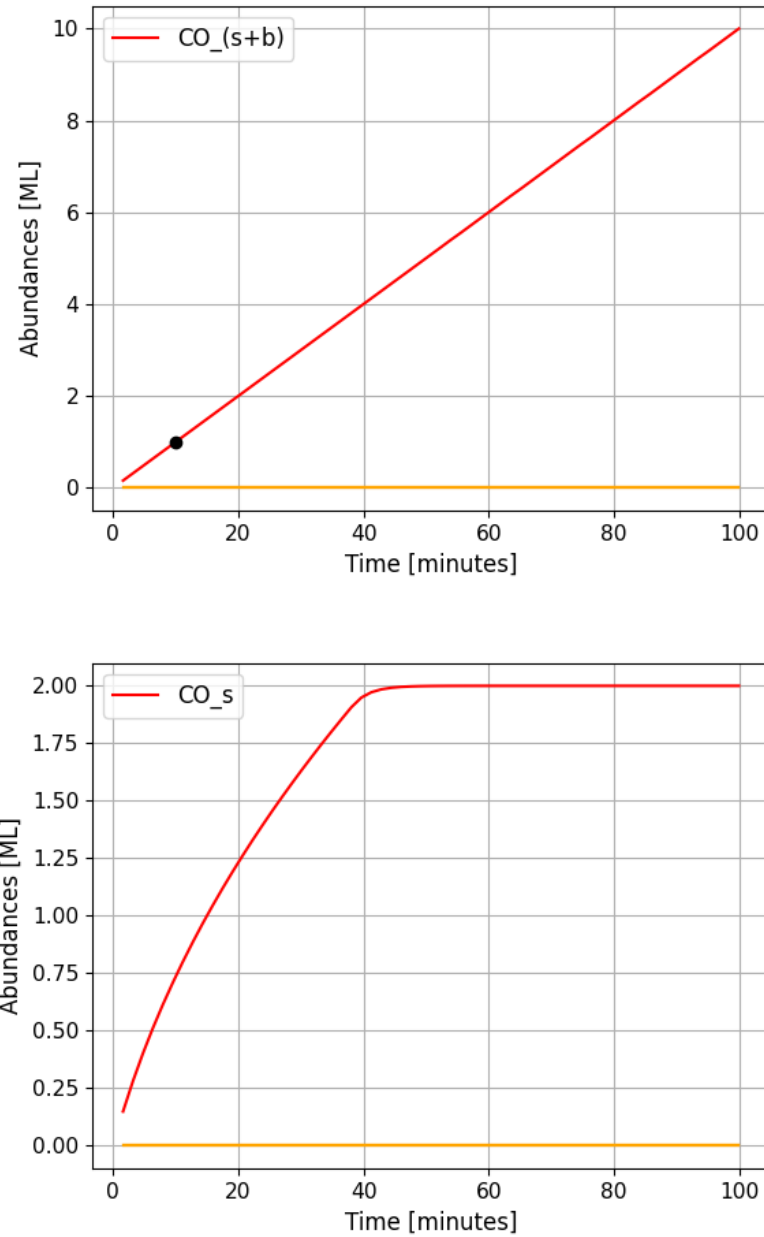


Figure 11: Experiment #1: Top panel : Growth of the CO ice on the surface, using the NAUTILUS code. CO_(s+b) denotes molecules from bulk and surface together. Bottom panel : Saturation of the chemical layer, the active layer is equal to 2. Black dot shows results from the experiments, where 1 ML of CO on the surface is obtained in 10 minutes.

Table 7: Results of simulations with the NAUTILUS code for $\{\text{CO} + \text{H}\}$ 60 min deposition with different surface temperatures (Experiments #4-#8). Tunnelling diffusion of H is turned off.

| Experiment | T (K) | CO | HCO | H_2CO | CH_2OH | CH_3O | CH_3OH |
|------------|----------|-------|-------|-----------------------|------------------------|-----------------------|------------------------|
| | | | | | (ML) | | |
| #4 | 9 | 2.848 | 1.888 | 1.318 | 0.0576 | 0.277 | 0.203 |
| #5 | 10 | 2.863 | 1.856 | 1.329 | 0.057 | 0.255 | 0.230 |
| #6 | 11 | 3.070 | 1.643 | 1.306 | 0.049 | 0.240 | 0.279 |
| #7 | 12 | 3.662 | 1.105 | 1.226 | 0.030 | 0.178 | 0.382 |
| #8 | 15 | 5.098 | 0.118 | 1.033 | 0.001 | 0.011 | 0.307 |

Table 8: Results of simulations with the NAUTILUS code for $\{\text{CO} + \text{H}\}$ 60 min deposition with different surface temperatures (Experiments #4-#8). Tunnelling of H diffusion is turned on; the diffusion barrier thickness is 3.5×10^{-8} cm.

| Experiment | T (K) | CO | HCO | H_2CO | CH_2OH | CH_3O | CH_3OH |
|------------|----------|-------|-------|-----------------------|------------------------|-----------------------|------------------------|
| | | | | | (ML) | | |
| #4 | 9 | 2.964 | 1.750 | 1.319 | 0.053 | 0.247 | 0.256 |
| #5 | 10 | 2.964 | 1.750 | 1.319 | 0.053 | 0.247 | 0.256 |
| #6 | 11 | 3.070 | 1.643 | 1.306 | 0.049 | 0.240 | 0.279 |
| #7 | 12 | 3.662 | 1.105 | 1.226 | 0.030 | 0.178 | 0.382 |
| #8 | 15 | 5.098 | 0.118 | 1.033 | 0.001 | 0.011 | 0.307 |

with the fiducial NAUTILUS input parameters, including the hydrogen diffusion parameters. We find the same general trends:

- almost no temperature dependency;
- a moderate overestimation of the molecules on the surface, indicating low efficiency of the chemical desorption process (independent of the H flux), compared to the experimental efficiency;
- an overabundance of radical intermediates.

In the Nautilus code, the hydrogen diffusion treatment can be set to only thermal hopping or both tunneling and hopping. The width of the barrier diffusion for H can be changed so that the ratio between thermal hopping and tunneling can be adapted.

Tables 6, and 8 show the results of changing the diffusion parameters of H. In the first case, when the diffusion is only thermal, a temperature dependence is observed. In the second case, we

keep the tunneling diffusion, but enlarge the diffusion barrier width to 3.5 Å, so that we increase the crossover temperature. As expected, the model results are closer to the thermal diffusion case only, but with some modifications at the lowest temperatures.

However, while these tests illustrate the great importance of H diffusion, they nevertheless show that it is not enough to modify these parameters to resolve the entire successive chemical chain, which depends above all on the number density of H on the surface, and therefore on its diffusion. This is somewhat counterintuitive, but the more H diffuses, the more it reforms H₂, and the lower its number density, and therefore the less effective the successive hydrogenation of CO, which has an entry barrier. We have also performed a full minimization of the reaction barrier parameters and found the best values, which are compatible with the values constrained in the previous section using the MONACO code.

pyRate code and results

pyRate is a rate-equation based astrochemical code that simulates the gas-grain chemical interaction occurring through adsorption and several desorption mechanisms. As described in detail in,¹² pyRate follows the time evolution of the abundances and reactions of chemical species with chemical networks developed to track the spin states of several species (H₂, H₂⁺, H₃⁺, NH₃, and H₂O; Sipilä et al.^{12, 82, 83}). Grain-size distributions can also be considered.⁸⁴ Like MONACO and Nautilus, the three-phase model (gas/surface/mantle) is considered for the experiment by co-deposition (experiments #1-8), where the reactive surface is defined at one layer but with no diffusion and reactivity in the mantle.⁶¹ The two-phase model (gas/solid) is used for the hydrogenation of pre-deposited CO ice experiment (experiment #9 and #10) because the abundance of species in the solid-phase is less than one monolayer.

For the following calculation, we use the same physical parameters as those described previously in Section Rate-equations approach, with some differences. The hydrogen number density n_{H} is set at $5 \times 10^{10} \text{ cm}^{-3}$. The probability of a reaction via diffusion is set at one for radical-radical

reactions, or can be calculated by tunnelling effect, with the chemical network summarised in Table 2 (the column $E_P R$ summarizes energies used in the code). The width of the tunnelling barrier for diffusion and reaction is assumed to be one. Reaction-diffusion-competition can be included or ignored. Chemical desorption is estimated using Riedel's equation,⁸⁵ a modified form of equation 9, in which the excess energy from the reaction is distributed among the products according to their mass.

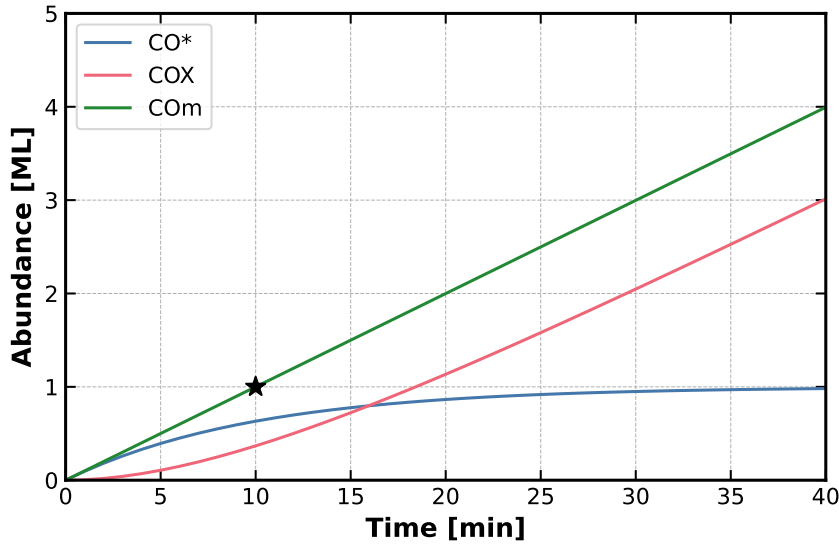


Figure 12: Experiment #1: Growth of CO ice on the substrate, case of pyRate code. The blue curve designated as CO^* illustrates the CO molecules located on the surface, while the red curve labeled COX indicates the CO molecules present within the bulk. The green curve, labeled COm , represents the sum of the CO molecule present on the surface and in the bulk. The black star represents results from the experiments #1.

In the case of the pyRate code, beam flux calibration was performed by measuring the time needed for a monolayer of the species to be completed on the grain surface, which was done by adjusting the initial abundances accordingly. All possible surface reactions were turned off during this calibration. The initial abundances were adjusted until they reached $n(\text{CO})/n_{\text{H}} = 4.203 \times 10^{-3}$ and $n(\text{CO})/n_{\text{H}} = 4.669 \times 10^{-3}$ for CO in experiments #1-2 and #3-10, respectively. These values correspond to deposition times of 10 minutes for a monolayer in the first set (see Figure 12) and 9 minutes in the second. For atomic hydrogen, the initial abundances were $n(\text{H})/n_{\text{H}} = 7.676 \times 10^{-3}$ for experiments #1-2 and $n(\text{H})/n_{\text{H}} = 3.839 \times 10^{-3}$ for experiments #3-10, considering a sticking

coefficient of 0.41.⁶⁵ The sticking coefficient of CO is around 1 in the experimental conditions.⁶⁶

Table 9: pyRate results with tunnelling diffusion and no reaction-diffusion competition.

| # | T (K) | Time (minutes) | CO | H ₂ CO | CH ₃ OH | Missing (ML) | HCO | CH ₂ OH | CH ₃ O |
|----|----------|-------------------|-----------|-------------------|--------------------|-----------------|-----------|--------------------|-------------------|
| 1 | 10 | 15 | 1.500(+0) | | | | | | |
| 2 | 10 | 15 | 1.433(+0) | 2.788(-2) | 5.729(-5) | 3.860(-2) | 7.666(-8) | 1.173(-12) | 1.617(-10) |
| 3 | 15 | 60 | 6.667(+0) | | | | | | |
| 4 | 9 | 60 | 6.329(+0) | 1.403(-1) | 3.864(-4) | 1.976(-1) | 3.388(-7) | 7.907(-12) | 8.135(-10) |
| 5 | 10 | 60 | 6.328(+0) | 1.403(-1) | 3.862(-4) | 1.979(-1) | 3.388(-7) | 7.904(-12) | 8.133(-10) |
| 6 | 11 | 60 | 6.328(+0) | 1.402(-1) | 3.860(-4) | 1.983(-1) | 3.388(-7) | 7.900(-12) | 8.131(-10) |
| 7 | 12 | 60 | 6.328(+0) | 1.402(-1) | 3.859(-4) | 1.988(-1) | 3.388(-7) | 7.896(-12) | 8.129(-10) |
| 8 | 15 | 60 | 6.326(+0) | 1.401(-1) | 3.853(-4) | 2.008(-1) | 3.387(-7) | 7.886(-12) | 8.123(-10) |
| 9 | 9 | 9+120 | 4.574(-1) | 2.271(-1) | 5.426(-3) | 3.101(-1) | 2.463(-8) | 1.108(-10) | 1.319(-9) |
| 10 | 9 | 9+75 | 6.128(-1) | 1.649(-1) | 2.390(-3) | 2.200(-1) | 3.291(-8) | 4.883(-11) | 9.567(-10) |

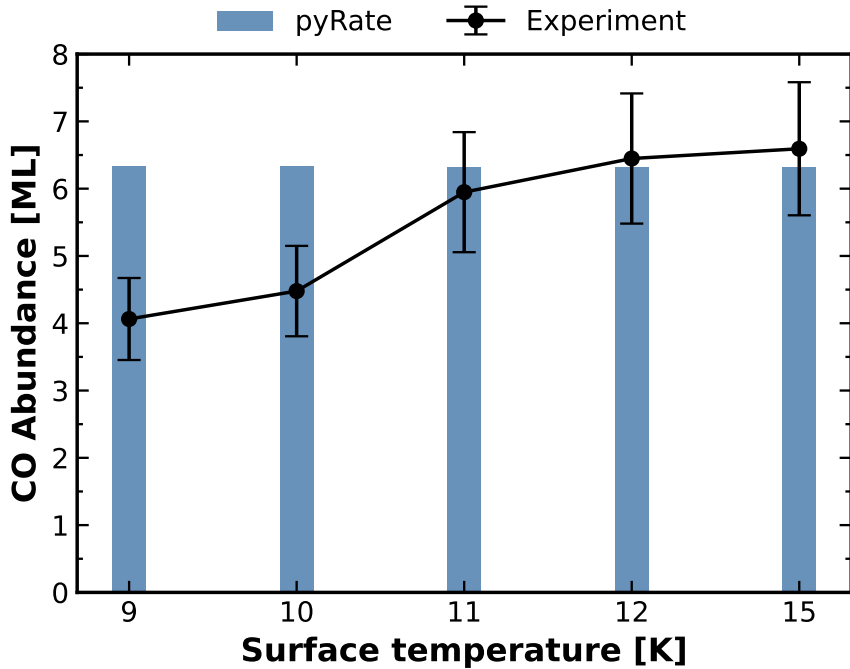


Figure 13: Solid-phase CO abundance as a function of surface temperature after 60 minutes of $\{\text{CO} + \text{H}\}$ co-deposition (experiments #4-8). The blue bar shows the predictions from the pyRate simulation (Table 9), while the black dots connected by lines indicate the experimental result (Table 1).

The results obtained with pyRate for experiments #1 to #10 are presented in Table 9 with tunnelling diffusion and without reaction-diffusion competition. Figure 13 illustrates the CO abundance in the solid phase as a function of surface temperature during CO and H co-deposition

experiments (#4-8). The pyRate predictions (represented by the blue bar) suggest a temperature-independent CO abundance in the solid phase of ~ 6.329 ML between 9 and 15 K. In contrast, the experimental measurements (black dots connected by lines) reveal a clear temperature dependence, with CO abundances of 4.063 ML at 9 K and 6.593 ML at 15 K. This discrepancy results from how the model handles reactivity and diffusion processes, which were both calculated with the tunnelling effect. Tunnelling in chemical reactions depends primarily on the mass of the involved species, and on the width and energy of the potential barrier. For the $\text{CO} + \text{H} \longrightarrow \text{HCO}$ reaction, Andersson et al.⁸⁶ has demonstrated theoretically that tunnelling dominates at temperatures below 181.8 K in the gas-phase. In addition, Rimola et al.²⁹ has shown theoretically that in the solid phase, within clusters of water molecules, the crossover temperature is 141 K for $\text{CO} + \text{H} \longrightarrow \text{HCO}$ and 181 K for $\text{H}_2\text{CO} + \text{H} \longrightarrow \text{CH}_3\text{O}$, which allows us to conclude that the tunnelling effect dominates the entire $\text{CO} + \text{H}$ chemical network in our experimental conditions. This is why we attribute the temperature dependence to thermal diffusion coupled with competitive reaction-diffusion processes. Thermal diffusion, which follows an Arrhenius law, increases exponentially with temperature. Conversely, the competitive reaction-diffusion mechanism, proposed by Garrod and Pauly⁸¹, suggests that if the migration time is shorter than the reaction time, there is a non-zero probability that a reactant may migrate to a different site instead of reacting with another species. Therefore, the higher the temperature, the faster H atoms diffuse and the less they react with CO. The probability for species A and B to react and form a species AB is described as follows:

$$p_{AB} = \begin{cases} \kappa_{AB} & \text{no competition,} \\ \frac{\nu_{AB}\kappa_{AB}}{\nu_{AB}\kappa_{AB} + k_{\text{diff}}(A) + k_{\text{diff}}(B)} & \text{with competition,} \end{cases} \quad (11)$$

where ν_{AB} is the highest characteristic frequency between reactant A and B, κ_{AB} the reaction probability from Hasegawa et al.⁶⁰, and k_{diff} the diffusion rate coefficient. The results from MONACO and NAUTILUS (Tables 5 and 7) show that the reaction-diffusion competition coupled with thermal hopping diffusion follows the temperature dependence of CO abundance observed in the experimental data (Table 1). However, this approach also presents additional issues.

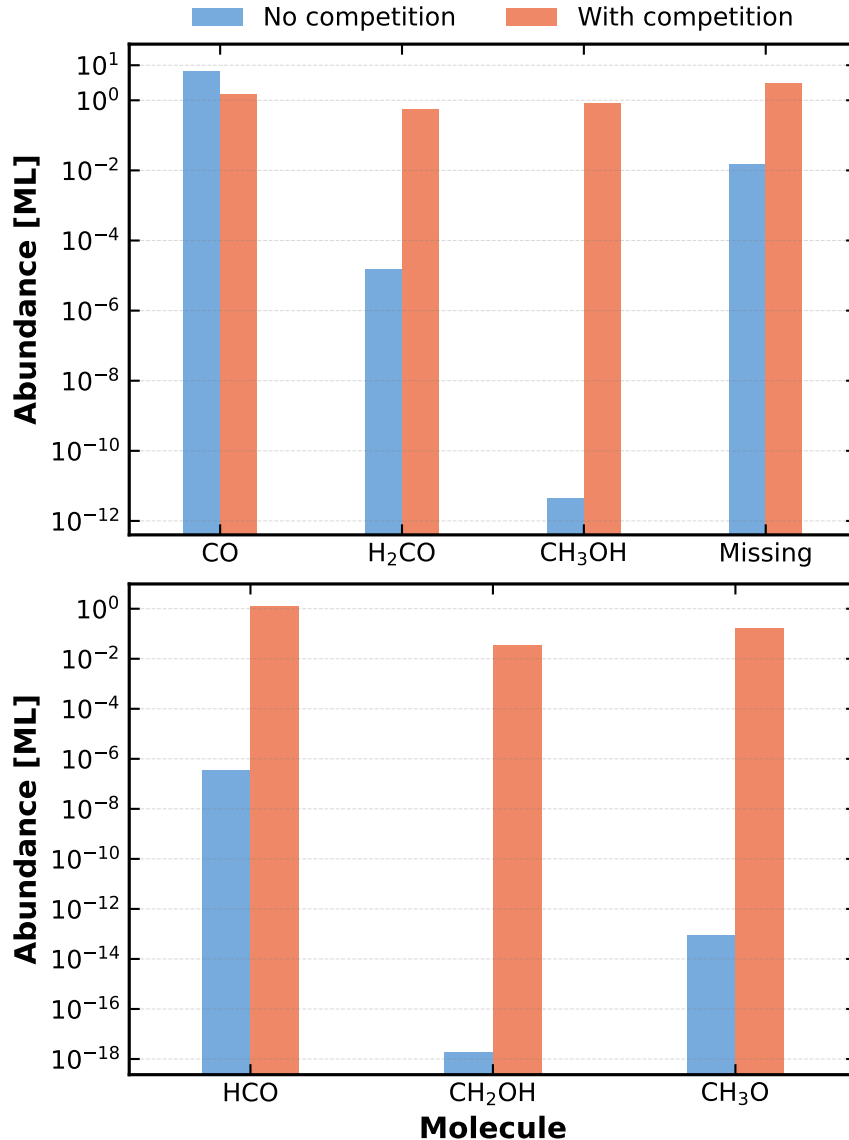


Figure 14: Results of pyRate simulations for $\{\text{CO} + \text{H}\}$ co-deposition at a surface temperature of 10 K (experiment #5) with thermal hopping diffusion. The data are presented for scenarios without reaction-diffusion competition (blue bar) and with reaction-diffusion competition (orange bar). The top panel shows the solid-phase abundances of detectable molecules (CO, H₂CO, and CH₃OH), where "Missing" indicates molecules absent from the solid-phase due to chemical desorption. The bottom panel illustrates the solid-phase abundances of radicals produced through CO reacting with H, especially HCO, CH₂OH, and CH₃O, which are not detected in the experiment.

Figure 14 presents the pyRate results for experiment #5, comparing scenarios with no reaction-diffusion competition (blue) and with competition (orange), while maintaining the same physical parameters. Thermal hopping diffusion is also considered. The results indicate that H atoms ex-

hibit increased reactivity with CO molecules under diffusion-reaction competition conditions, with 1.525 ML of CO remaining on the solid-phase at the end of the co-deposition {CO + H}, compared to 6.352 ML in its absence. This trend is also observed for other products: 0.5569 ML of H₂CO, 0.8157 ML of CH₃OH, and 3.038 ML for the missing column (chemical desorption) when competition is considered, compared to 1.541×10^{-5} ML, 4.459×10^{-12} ML, and 1.487×10^{-2} ML without competition, respectively. Regarding radicals, a notable difference in their estimated abundances is observed when employing the competition method, with HCO reaching up to 1.257 ML. Given this abundance, HCO should be detectable through IR spectroscopy during the experiments, however, such detection is not observed (see Figure 5).

A closer look at equation 11 for the CO + H \longrightarrow HCO reaction reveals that the reaction coefficient rate $\nu_{AB}\kappa_{AB}$, estimated approximately at 1.8×10^5 s⁻¹ for a barrier of 1730 K, is much higher than the diffusion coefficient rates k_{diff} of H atoms and CO molecules, estimated approximately at 6.0×10^1 and 2.8×10^{-21} s⁻¹, respectively. With a reaction coefficient that is approximately four orders of magnitude greater than hydrogen diffusion, equation 11 predicts a probability near unity when the reaction-diffusion competition is used. Thus, the inclusion of the diffusion-reaction competition makes the reaction "barrierless" and leads to an over-reactivity of CO with H. Therefore, all H atoms mainly react with CO and less frequently with other molecules, since CO is present everywhere on the surface as co-deposited with H.

Reaction-diffusion competition currently does not address the experimental question. It effectively reproduces the temperature dependence, suggesting an interaction between reactivity and surface processes, mainly diffusion at low temperatures. However, in regimes where diffusion is slower than reactivity, the model tends to overestimate the reaction probability.

Conclusion

This study has shown that rate-equation codes such as MONACO, NAUTILUS, and pyRate can be used to simulate experimental conditions without the need to change the programming structure of

dedicated computer codes. It simply requires a good understanding and proper adjustment of the physical parameters in models, and for experimentalists — a clear description of the experimental parameters and observables. At 10 K, adjusting the H diffusion property in any model is enough to obtain a fair reproduction of the experimental data. However, our attempts to reproduce the temperature dependency showed that the quantum tunneling crossover temperature appears to be lower or the quantum diffusion of H atoms at 10 K is overestimated. Using thermal hopping for H atoms only allowed us to adjust reaction parameters to finally achieve a reasonably good match of the experiments, with two notable deviations: the underestimation of the chemical desorption and the overabundance of radicals proposed in the models. To accurately reproduce the surface temperature dependence, reaction-diffusion competition and thermal hopping diffusion must be incorporated. However, reaction-diffusion-competition results in over-reactivity when the diffusion coefficient rate is lower than the reaction coefficient rate, leading to an excess of radicals.

This exploratory work shows us that both modellers and experimentalists can compare their approaches, providing the former with a robust model and the latter with unprecedented access to the details of the processes at work in the experiments.

After 18 months of parallel and complementary work, some points stand out very clearly. For experiments, in addition to an unambiguous description, it is crucial to have a coherent quantitative dataset, as complete as possible, not only on observables (deposited species, formed species including upper limits for radicals), but also on experimental parameters. In this study, we found that the surface temperature is very important, but the fluxes could also add valuable constraints for modellers. It would also be good to probe different chemical regimes (barrierless or not) and to propose layered experiments to test the molecule transfer from surface to bulk and vice versa, which are yet to be compared with models.

Before examining the details of chemical networks and their barriers, it seems that the key point lies in the diffusion of hydrogen and its intertwining with certain model assumptions, particularly the diffusion-reaction competition. In the case of hydrogenation reactions, these are an essential step in validation. To this end, experiments with different entrance barriers would impose different

constraints and would undoubtedly help to tackle this issue. Adjusting reaction efficiencies does not seem to be a problem if the scope of conditions is large enough. It is likely that the importance of Eley-Rideal processes, for example, can also be addressed, since it is easy to vary the initial coverage and to test the hypothesis.

Acknowledgement

This project was supported by the Programme National “Physique et Chimie du Milieu Interstellaire” (PCMI) of CNRS/INSU with INC/INP co-funded by Commissariat à l’Energie Atomique (CEA) and Centre National d’Etudes Spatiales (CNES). This work was supported by the Agence Nationale de la Recherche (ANR) SIRC project (Grant ANR-SPV202448 2020-2024). AV work was supported by the contract FEUZ-2025-0003. The authors would like to thank Julie Vitorino and Saoud Baouche for their help with the experiments conducted for this project at the CY LIRA laboratory.

Supporting Information Available

References

- (1) Tielens, A. G. G. M. *The physics and chemistry of the interstellar medium*; Cambridge University Press: New York, 2005.
- (2) McClure, M. K. et al. An Ice Age JWST inventory of dense molecular cloud ices. *Nat. Astron.* **2023**, *7*, 431–443.
- (3) Rocha, W. R. M. et al. JWST Observations of Young protoStars (JOYS+): Detecting icy complex organic molecules and ions. I. CH₄, SO₂, HCOO[−], OCN[−], H₂CO, HCOOH, CH₃CH₂OH, CH₃CHO, CH₃OCHO, and CH₃COOH. *Astron. Astrophys.* **2024**, *683*, A124.

(4) Nazari, P. et al. Hunting for complex cyanides in protostellar ices with the JWST. A tentative detection of CH₃CN and C₂H₅CN. *Astron. Astrophys.* **2024**, *686*, A71.

(5) Martín-Doménech, R.; Rivilla, V. M.; Jiménez-Serra, I.; Quénard, D.; Testi, L.; Martín-Pintado, J. Detection of methyl isocyanate (CH₃NCO) in a solar-type protostar. *Mon. Not. R. Astron. Soc.* **2017**, *469*, 2230–2234.

(6) Codella, C. et al. Seeds of Life in Space (SOLIS). II. Formamide in protostellar shocks: Evidence for gas-phase formation. *Astron. Astrophys.* **2017**, *605*, L3.

(7) Vastel, C. et al. FAUST. XI. Enhancement of the complex organic material in the shocked matter surrounding the [BHB2007] 11 protobinary system. *Astron. Astrophys.* **2024**, *684*, A189.

(8) Tu, T.-Y.; Wakelam, V.; Chen, Y.; Zhou, P.; Zhang, Q.-Q. Molecular chemistry induced by a J-shock toward supernova remnant W51C. *Astron. Astrophys.* **2025**, *693*, A222.

(9) Vasyunin, A. I.; Caselli, P.; Dulieu, F.; Jiménez-Serra, I. Formation of Complex Molecules in Prestellar Cores: A Multilayer Approach. *Astrophys. J.* **2017**, *842*, 33.

(10) Bergantini, A.; Zhu, C.; Kaiser, R. I. A Photoionization Reflectron Time-of-flight Mass Spectrometric Study on the Formation of Acetic Acid (CH₃COOH) in Interstellar Analog Ices. *Astrophys. J.* **2018**, *862*, 140.

(11) Perrero, J.; Beitia-Antero, L.; Fuente, A.; Ugliengo, P.; Rimola, A. Theoretical modelling of the adsorption of neutral and charged sulphur-bearing species on to olivine nanoclusters. *Mon. Not. R. Astron. Soc.* **2023**, *527*, 10697–10704.

(12) Sipilä, O.; Caselli, P.; Harju, J. Benchmarking spin-state chemistry in starless core models. *Astron. Astrophys.* **2015**, *578*, A55.

(13) Ruaud, M.; Wakelam, V.; Hersant, F. Gas and grain chemical composition in cold cores as

predicted by the Nautilus three-phase model. *Mon. Not. R. Astron. Soc.* **2016**, *459*, 3756–3767.

(14) Jiménez-Serra, I. et al. Modelling methanol and hydride formation in the JWST Ice Age era. *Astron. Astrophys.* **2025**, *695*, A247.

(15) Fedoseev, G.; Cuppen, H. M.; Ioppolo, S.; Lamberts, T.; Linnartz, H. Experimental evidence for glycolaldehyde and ethylene glycol formation by surface hydrogenation of CO molecules under dense molecular cloud conditions. *Mon. Not. R. Astron. Soc.* **2015**, *448*, 1288–1297.

(16) Chuang, K.-J.; Fedoseev, G.; Ioppolo, S.; van Dishoeck, E. F.; Linnartz, H. H-atom addition and abstraction reactions in mixed CO, H₂CO and CH₃OH ices - an extended view on complex organic molecule formation. *Mon. Not. R. Astron. Soc.* **2016**, *455*, 1702–1712.

(17) Kruczakiewicz, F.; Vitorino, J.; Congiu, E.; Theulé, P.; Dulieu, F. Ammonia snow lines and ammonium salts desorption. *Astron. Astrophys.* **2021**, *652*, A29.

(18) Nakibov, R.; Karteyeva, V.; Petrushkevich, I.; Ozhiganov, M.; Medvedev, M.; Vasyunin, A. Solid and Gaseous Methane in IRAS 23385+6053 as Seen with Open JWST Data. *Astrophys. J. Lett.* **2025**, *978*, L46.

(19) Ozhiganov, M.; Medvedev, M.; Karteyeva, V.; Nakibov, R.; Sapunova, U.; Krushinsky, V.; Stepanova, K.; Tryastsina, A.; Gorkovenko, A.; Fedoseev, G.; Vasyunin, A. Infrared Spectra of Solid HCN Embedded in Various Molecular Environments for Comparison with the Data Obtained with JWST. *Astrophys. J. Lett.* **2024**, *972*, L10.

(20) Cazaux, S.; Martín-Doménech, R.; Chen, Y. J.; Muñoz Caro, G. M.; González Díaz, C. CO Depletion: A Microscopic Perspective. *Astrophys. J.* **2017**, *849*, 80.

(21) van Dishoeck, E. F. Astrochemistry: overview and challenges. Astrochemistry VII: Through the Cosmos from Galaxies to Planets. 2018; pp 3–22.

(22) Schlemmer, S.; Giesen, T.; Mutschke, H. *Laboratory Astrochemistry: From Molecules through Nanoparticles to Grains*; Wiley, 2015.

(23) Perrero, J.; Vitorino, J.; Congiu, E.; Ugliengo, P.; Rimola, A.; Dulieu, F. Binding energies of ethanol and ethylamine on interstellar water ices: synergy between theory and experiments. *Phys. Chem. Chem. Phys.* **2024**, *26*, 18205–18222.

(24) McElroy, D.; Walsh, C.; Markwick, A. J.; Cordiner, M. A.; Smith, K.; Millar, T. J. The UMIST database for astrochemistry 2012. *Astron. Astrophys.* **2013**, *550*, A36.

(25) Millar, T. J.; Walsh, C.; Van de Sande, M.; Markwick, A. J. The UMIST Database for Astrochemistry 2022. *Astron. Astrophys.* **2024**, *682*, A109.

(26) Wakelam, V. et al. A KInetic Database for Astrochemistry (KIDA). *Astrophys. J. Suppl. Ser.* **2012**, *199*, 21.

(27) Wakelam, V. et al. The 2014 KIDA Network for Interstellar Chemistry. *Astrophys. J. Suppl. Ser.* **2015**, *217*, 20.

(28) Wakelam, V.; Gratier, P.; Loison, J. C.; Hickson, K. M.; Penguen, J.; Mechineau, A. The 2024 KIDA network for interstellar chemistry. *Astron. Astrophys.* **2024**, *689*, A63.

(29) Rimola, A.; Taquet, V.; Ugliengo, P.; Balucani, N.; Ceccarelli, C. Combined quantum chemical and modeling study of CO hydrogenation on water ice. *Astron. Astrophys.* **2014**, *572*, A70.

(30) Hiraoka, K.; Sato, T.; Sato, S.; Sogoshi, N.; Yokoyama, T.; Takashima, H.; Kitagawa, S. Formation of Formaldehyde by the Tunneling Reaction of H with Solid CO at 10 K Revisited. *Astrophys. J.* **2002**, *577*, 265–270.

(31) Watanabe, N.; Nagaoka, A.; Shiraki, T.; Kouchi, A. Hydrogenation of CO on Pure Solid CO and CO-H₂O Mixed Ice. *Astrophys. J.* **2004**, *616*, 638–642.

(32) Fuchs, G. W.; Cuppen, H. M.; Ioppolo, S.; Romanzin, C.; Bisschop, S. E.; Andersson, S.; van Dishoeck, E. F.; Linnartz, H. Hydrogenation reactions in interstellar CO ice analogues - A combined experimental/theoretical approach. *Astron. Astrophys.* **2009**, *505*, 629–639.

(33) Pirim, C.; Krim, L. An FTIR study on the catalytic effect of water molecules on the reaction of CO successive hydrogenation at 3 K. *Chem. Phys.* **2011**, *380*, 67–76.

(34) Minissale, M.; Moudens, A.; Baouche, S.; Chaabouni, H.; Dulieu, F. Hydrogenation of CO-bearing species on grains: unexpected chemical desorption of CO. *Mon. Not. R. Astron. Soc.* **2016**, *458*, 2953–2961.

(35) Fillion, J.-H.; Bertin, M.; Danger, G.; Duvernay, F.; Minissale, M. Complex organic molecules and interstellar ices: recent progresses from laboratory astrophysics. SF2A-2018: Proceedings of the Annual meeting of the French Society of Astronomy and Astrophysics. 2018; pp 15–19.

(36) Dartois, E.; Chabot, M.; Bacmann, A.; Boduch, P.; Domaracka, A.; Rothard, H. Non-thermal desorption of complex organic molecules. Cosmic-ray sputtering of CH_3OH embedded in CO_2 ice. *Astron. Astrophys.* **2020**, *634*, A103.

(37) Pantaleone, S.; Enrique-Romero, J.; Ceccarelli, C.; Ugliengo, P.; Balucani, N.; Rimola, A. Chemical Desorption versus Energy Dissipation: Insights from Ab Initio Molecular Dynamics of HCO^\cdot Formation. *Astrophys. J.* **2020**, *897*, 56.

(38) Morisset, S.; Rougeau, N.; Teillet-Billy, D. Hydrogenation reactions and adsorption : From CO to methanol on a graphene surface. *Mol. Astrophys.* **2019**, *14*, 1–9.

(39) Enrique-Romero, J.; Ceccarelli, C.; Rimola, A.; Skouteris, D.; Balucani, N.; Ugliengo, P. Theoretical computations on the efficiency of acetaldehyde formation on interstellar icy grains. *Astron. Astrophys.* **2021**, *655*, A9.

(40) Enrique-Romero, J.; Rimola, A.; Ceccarelli, C.; Ugliengo, P.; Balucani, N.; Skouteris, D. Quantum Mechanical Simulations of the Radical-Radical Chemistry on Icy Surfaces. *Astrophys. J. Suppl. Ser.* **2022**, 259, 39.

(41) Jin, M.; Garrod, R. T. Formation of Complex Organic Molecules in Cold Interstellar Environments through Nondiffusive Grain-surface and Ice-mantle Chemistry. *Astrophys. J. Suppl. Ser.* **2020**, 249, 26.

(42) Spezzano, S.; Fuente, A.; Caselli, P.; Vasyunin, A.; Navarro-Almaida, D.; Rodríguez-Baras, M.; Punanova, A.; Vastel, C.; Wakelam, V. Gas phase Elemental abundances in Molecular cloudS (GEMS) V. Methanol in Taurus. *Astron. Astrophys.* **2022**, 657, A10.

(43) Jiménez-Serra, I.; Vasyunin, A. I.; Spezzano, S.; Caselli, P.; Cosentino, G.; Viti, S. The Complex Organic Molecular Content in the L1498 Starless Core. *Astrophys. J.* **2021**, 917, 44.

(44) Megías, A.; Jiménez-Serra, I.; Martín-Pintado, J.; Vasyunin, A. I.; Spezzano, S.; Caselli, P.; Cosentino, G.; Viti, S. The complex organic molecular content in the L1517B starless core. *Mon. Not. R. Astron. Soc.* **2022**, 519, 1601–1617.

(45) Congiu, E.; Sow, A.; Nguyen, T.; Baouche, S.; Dulieu, F. A new multi-beam apparatus for the study of surface chemistry routes to formation of complex organic molecules in space. *Rev. Sci. Instrum.* **2020**, 91.

(46) Husquinet, B.; Vitorino, J.; Sipilä, O.; Caselli, P.; Dulieu, F. Neon is an inhibitor of CO hydrogenation in pre-stellar core conditions. *Astron. Astrophys.* **2025**, 703, A16.

(47) Vitorino, J.; Loison, J. C.; Wakelam, V.; Congiu, E.; Dulieu, F. Sulphur storage in cold molecular clouds: the case of the NH_4^+SH^- salt on interstellar dust grains. *Mon. Not. R. Astron. Soc.* **2024**, 533, 52–62.

(48) Hwang, W.; Kim, Y.-K.; Rudd, M. E. New model for electron-impact ionization cross sections of molecules. *J. Chem. Phys.* **1996**, *104*, 2956–2966.

(49) Vinodkumar, M.; Bhutadia, H.; Limbachiya, C.; Joshipura, K. Electron impact total ionization cross sections for H₂S, PH₃, HCHO and HCOOH. *Int. J. Mass Spectrom.* **2011**, *308*, 35–40.

(50) Kumar, Y.; Kumar, M.; Kumar, S.; Kumar, R. The Electron Impact Ionization Cross Sections of Methanol, Ethanol and 1-Propanol. *Atoms* **2019**, *7*, 60.

(51) Krucziewicz, F.; Dulieu, F.; Ivlev, A. V.; Caselli, P.; Giuliano, B. M.; Ceccarelli, C.; Theulé, P. Comprehensive laboratory constraints on thermal desorption of interstellar ice analogues. *Astron. Astrophys.* **2024**, *686*, A236.

(52) Congiu, E.; Fedoseev, G.; Ioppolo, S.; Dulieu, F.; Chaabouni, H.; Baouche, S.; Lemaire, J. L.; Laffon, C.; Parent, P.; Lamberts, T.; Cuppen, H. M.; Linnartz, H. No Ice Hydrogenation: A Solid Pathway to NH₂OH Formation in Space. *Astrophys. J.l* **2012**, *750*, L12.

(53) Dulieu, F.; Congiu, E.; Noble, J.; Baouche, S.; Chaabouni, H.; Moudens, A.; Minissale, M.; Cazaux, S. How micron-sized dust particles determine the chemistry of our Universe. *Sci. Rep.* **2013**, *3*, 1338.

(54) Gerakines, P. A.; Materese, C. K.; Hudson, R. L. Carbon monoxide ices - a semicentennial review and update for crystalline CO along with the first IR spectrum and band strength for amorphous CO. *Mon. Not. R. Astron. Soc.* **2023**, *522*, 3145–3162.

(55) Ryazantsev, S. V.; Tyurin, D. A.; Feldman, V. I. Experimental determination of the absolute infrared absorption intensities of formyl radical HCO. *Spectrochimica Acta Part A: Molecular Spectroscopy* **2017**, *187*, 39–42.

(56) Zhitnikov, R. A.; Dmitriev, Y. A. Detection of free radicals in low-temperature gas-grain reactions of astrophysical interest. *Astron. Astrophys.* **2002**, *386*, 1129–1138.

(57) Butscher, T.; Duvernay, F.; Theule, P.; Danger, G.; Carissan, Y.; Hagebaum-Reignier, D.; Chiavassa, T. Formation mechanism of glycolaldehyde and ethylene glycol in astrophysical ices from $\text{HCO}\bullet$ and $\bullet\text{CH}_2\text{OH}$ recombination: an experimental study. *Mon. Not. R. Astron. Soc.* **2015**, *453*, 1587–1596.

(58) Cuppen, H. M.; Linnartz, H.; Ioppolo, S. Laboratory and Computational Studies of Interstellar Ices. *arXiv e-prints* **2024**, arXiv:2407.06657.

(59) Vasyunin, A. I.; Herbst, E. Reactive Desorption and Radiative Association as Possible Drivers of Complex Molecule Formation in the Cold Interstellar Medium. *Astrophys. J.* **2013**, *769*, 34.

(60) Hasegawa, T. I.; Herbst, E.; Leung, C. M. Models of Gas-Grain Chemistry in Dense Interstellar Clouds with Complex Organic Molecules. *Astrophys. J. Suppl. Ser.* **1992**, *82*, 167.

(61) Hasegawa, T. I.; Herbst, E. Three-Phase Chemical Models of Dense Interstellar Clouds - Gas Dust Particle Mantles and Dust Particle Surfaces. *Mon. Not. R. Astron. Soc.* **1993**, *263*, 589.

(62) Garrod, R. T.; Widicus Weaver, S. L.; Herbst, E. Complex Chemistry in Star-forming Regions: An Expanded Gas-Grain Warm-up Chemical Model. *Astrophys. J.* **2008**, *682*, 283–302.

(63) Caselli, P.; Hasegawa, T. I.; Herbst, E. The Production of Condensed Phase CO in Quiescent Molecular Clouds. *Astrophys. J.* **1994**, *421*, 206.

(64) Vasyunin, A. I.; Semenov, D. A.; Wiebe, D. S.; Henning, T. A Unified Monte Carlo Treatment of Gas-Grain Chemistry for Large Reaction Networks. I. Testing Validity of Rate Equations in Molecular Clouds. *Astrophys. J.* **2009**, *691*, 1459–1469.

(65) Cuppen, H. M.; Kristensen, L. E.; Gavardi, E. H_2 reformation in post-shock regions. *Mon. Not. R. Astron. Soc.* **2010**, *406*, L11–L15.

(66) He, J.; Acharyya, K.; Vidali, G. Sticking of molecules on nonporous amorphous water ice. *Astrophys. J.* **2016**, *823*, 56.

(67) Garrod, R. T. A new modified-rate approach for gas-grain chemical simulations. *Astron. Astrophys.* **2008**, *491*, 239–251.

(68) Garrod, R. T.; Vasyunin, A. I.; Semenov, D. A.; Wiebe, D. S.; Henning, T. A New Modified-Rate Approach For Gas-Grain Chemistry: Comparison with a Unified Large-Scale Monte Carlo Simulation. *Astrophys. J. Lett.* **2009**, *700*, L43–L46.

(69) Hollenbach, D.; McKee, C. F. Molecule formation and infrared emission in fast interstellar shocks. I. Physical processes. *Astrophys. J. Suppl. Ser.* **1979**, *41*, 555–592.

(70) Senevirathne, B.; Andersson, S.; Dulieu, F.; Nyman, G. Hydrogen atom mobility, kinetic isotope effects and tunneling on interstellar ices (I_h and ASW). *Mol. Astrophys.* **2017**, *6*, 59–69.

(71) Nyman, G. Tunneling of Hydrogen and Deuterium Atoms on Interstellar Ices (I_h and ASW). *Front. Astron. Space Sci.* **2021**, *8*.

(72) Minissale, M.; Dulieu, F.; Cazaux, S.; Hocuk, S. Dust as interstellar catalyst. I. Quantifying the chemical desorption process. *Astron. Astrophys.* **2016**, *585*, A24.

(73) Punanova, A. F.; Borshcheva, K.; Fedoseev, G. S.; Caselli, P.; Wiebe, D. S.; Vasyunin, A. I. Correlation between formaldehyde and methanol in prestellar cores. *Mon. Not. R. Astron. Soc.* **2025**, *537*, 3686–3700.

(74) Qasim, D.; Fedoseev, G.; Chuang, K. J.; Taquet, V.; Lamberts, T.; He, J.; Ioppolo, S.; van Dishoeck, E. F.; Linnartz, H. Formation of interstellar propanal and 1-propanol ice: a pathway involving solid-state CO hydrogenation. *Astron. Astrophys.* **2019**, *627*, A1.

(75) Garrod, R. T. A Three-phase Chemical Model of Hot Cores: The Formation of Glycine. *Astrophys. J.* **2013**, *765*, 60.

(76) Ligterink, N. F. W.; Walsh, C.; Cuppen, H. M.; Drozdovskaya, M. N.; Ahmad, A.; Benoit, D. M.; Carder, J. T.; Das, A.; Díaz-Berrios, J. K.; Dulieu, F.; Heyl, J.; Jardine, A.; Lamberts, T.; Mikkelsen, N. M.; Tsuge, M. Molecular mobility of extraterrestrial ices: surface diffusion in astrochemistry and planetary science. *Phys. Chem. Chem. Phys.* **2025**,

(77) Borshcheva, K.; Fedoseev, G.; Punanova, A. F.; Caselli, P.; Jiménez-Serra, I.; Vasyunin, A. I. Formation of Complex Organic Molecules in Prestellar Cores: The Role of Nondiffusive Grain Chemistry. *Astrophys. J.* **2025**, 990, 163.

(78) Minissale, M. et al. Thermal Desorption of Interstellar Ices: A Review on the Controlling Parameters and Their Implications from Snowlines to Chemical Complexity. *ACS Earth Space Chem.* **2022**, 6, 597–630.

(79) Ioppolo, S.; Fedoseev, G.; Chuang, K. J.; Cuppen, H. M.; Clements, A. R.; Jin, M.; Garrod, R. T.; Qasim, D.; Kofman, V.; van Dishoeck, E. F.; Linnartz, H. A non-energetic mechanism for glycine formation in the interstellar medium. *Nat. Astron.* **2021**, 5, 197–205.

(80) Chang, Q.; Cuppen, H. M.; Herbst, E. Gas-grain chemistry in cold interstellar cloud cores with a microscopic Monte Carlo approach to surface chemistry. *Astron. Astrophys.* **2007**, 469, 973–983.

(81) Garrod, R. T.; Pauly, T. On the Formation of CO₂ and Other Interstellar Ices. *Astrophys. J.* **2011**, 735, 15.

(82) Sipilä, O.; Caselli, P.; Harju, J. HD depletion in starless cores. *Astron. Astrophys.* **2013**, 554, A92.

(83) Sipilä, O.; Harju, J.; Caselli, P.; Schlemmer, S. Spin-state chemistry of deuterated ammonia. *Astron. Astrophys.* **2015**, 581, A122.

(84) Sipilä, O.; Zhao, B.; Caselli, P. Effect of grain size distribution and size-dependent grain

heating on molecular abundances in starless and pre-stellar cores. *Astron. Astrophys.* **2020**, *640*, A94.

- (85) Riedel, W.; Sipilä, O.; Redaelli, E.; Caselli, P.; Vasyunin, A.; Dulieu, F.; Watanabe, N. Modelling deuterated isotopologues of methanol towards the pre-stellar core L1544. *Astron. Astrophys.* **2023**, *680*, A87.
- (86) Andersson, S.; Goumans, T.; Arnaldsson, A. Tunneling in hydrogen and deuterium atom addition to CO at low temperatures. *Chem. Phys. Lett.* **2011**, *513*, 31–36.